Neuroimaging-AI endophenotypes reveal underlying mechanisms and genetic factors contributing to progression and development of four brain disorders

Junhao Wen[1,2,3,4,5,6,7*], Ioanna Skampardoni[8], Ye Ella Tian[9], Zhijian Yang[8], Yuhan Cui[8], Guray Erus[8], Gyujoon Hwang[8], Erdem Varol[10], Aleix Boquet-Pujadas[1], Ganesh B. Chand[11], Ilya Nasrallah[8], Theodore D. Satterthwaite[12], Haochang Shou[8,13], Li Shen[13], Arthur W. Toga[14], Andrew Zalesky[9], Christos Davatzikos[8,*]

[1]Laboratory of AI and Biomedical Science (LABS), Columbia University, New York, NY, USA
[2]Department of Radiology, Columbia University, New York, NY, USA
[3]New York Genome Center (NYGC), New York, NY, USA
[4]Department of Biomedical Engineering, Columbia University, New York, NY, USA
[5]Data Science Institute (DSI), Columbia University, New York, NY, USA
[6]Center for Innovation in Imaging Biomarkers and Integrated Diagnostics (CIMBID), Department of Radiology, Columbia University, New York, NY, USA
[7]Zuckerman Institute, Columbia University, New York, NY, USA
[8]Artificial Intelligence in Biomedical Imaging Laboratory (AIBIL), Center for AI and Data Science for Integrated Diagnostics (AI²D), Perelman School of Medicine, University of Pennsylvania, Philadelphia, USA
[9]Systems Lab, Department of Psychiatry, Melbourne Medical School, The University of Melbourne, Melbourne, Victoria, Australia
[10]Department of Computer Science and Engineering, New York University, New York, USA
[11]Department of Radiology, School of Medicine, Washington University in St. Louis, St. Louis, MO, USA
[12]Department of Psychiatry, Perelman School of Medicine, University of Pennsylvania, Philadelphia, USA
[13]Department of Biostatistics, Epidemiology and Informatics University of Pennsylvania Perelman School of Medicine, Philadelphia, USA
[14]Laboratory of Neuro Imaging (LONI), Stevens Neuroimaging and Informatics Institute, Keck School of Medicine of USC, University of Southern California, Los Angeles, California, USA

*Corresponding authors:
Junhao Wen, junhao.wen89@gmail.com
622 W 168th St, New York, NY 10032
Christos Davatzikos, christos.davatzikos@pennmedicine.upenn.edu
3700 Hamilton Walk, 7th Floor, Philadelphia, PA 19104, United States

1

Abstract

Recent work leveraging artificial intelligence has offered promise to dissect disease heterogeneity by identifying complex intermediate brain phenotypes, called dimensional neuroimaging endophenotypes (DNEs). We advance the argument that these DNEs capture the degree of expression of respective neuroanatomical patterns measured, offering a dimensional neuroanatomical representation for studying disease heterogeneity and similarities of neurologic and neuropsychiatric diseases. We investigate the presence of nine DNEs derived from independent yet harmonized studies on Alzheimer's disease, autism spectrum disorder, late-life depression, and schizophrenia in the UK Biobank study. Phenome-wide associations align with genome-wide associations, revealing 31 genomic loci (P-value$<5\text{x}10^{-8}/9$) associated with the nine DNEs.The nine DNEs, along with their polygenic risk scores, significantly enhanced the predictive accuracy for 14 systemic disease categories, particularly for conditions related to mental health and the central nervous system, as well as mortality outcomes. These findings underscore the potential of the nine DNEs to capture the expression of disease-related brain phenotypes in individuals of the general population and to relate such measures with genetics, lifestyle factors, and chronic diseases.

Main

Disease heterogeneity[1–8] has been a significant challenge for precision medicine[9]. A new era powered by artificial intelligence (AI) and large-scale, multi-omics biomarkers may enable us to quantify individualized liability for various brain diseases[10,11]. Recent work has leveraged semi-supervised clustering methods (**Fig. 1a** and **Supplementary Method 1**) to tackle this challenge. These methods characterize disease heterogeneity by constructing a mapping or transformation from a reference group, or healthy controls, to a target group, such as patients with a specific disease. In clinical neuroscience, these methods can quantify deviation from typical brain structure measured by T1-weighted magnetic resonance imaging (MRI)[12,2,1,13]. They represent disease-related neuroanatomical heterogeneity with multiple low-dimensional categorical subtypes associated with specific patterns of brain change relative to the reference group. Instead of focusing on the categorical subtypes, we investigated their corresponding continuous phenotypes (i.e., dimensions)[14], given that many chronic brain diseases develop along a continuous spectrum. Each neuroanatomical pattern's level of expression, therefore, serves as a dimensional AI-derived biomarker pertinent to the respective disease.

Previous heterogeneity research has primarily focused on within-disease heterogeneity[1–8]. However, this approach neglects the shared disease mechanisms, genetics, and clinical manifestations among different brain diseases. Conversely, while several studies have investigated the shared genetic components across various brain diseases, they have overlooked the important aspect of disease heterogeneity within each condition[15,16]. As such, a broad perspective is required to investigate disease heterogeneity simultaneously, spanning multiple neurodegenerative and neuropsychiatric disorders. This holistic approach aids in understanding the commonalities and interrelationships between these brain diseases and the multi-organ systems of humans[17,18]. Such an effort could simultaneously capture neurobiological heterogeneity within disorders and explain shared features, mechanisms, and risk factors across disorders. Ultimately, unraveling neurobiological heterogeneity within neuropsychiatric syndromes and explaining co-morbidity among them promises to accelerate more effective diagnosis, treatment, and prevention strategies.

These AI-derived biomarkers capture disease-specific neuroanatomic heterogeneity. However, whether these biomarkers are present in the general population, potentially simultaneously, remains unknown. Here, we sought to measure the presence of multiple AI-based signatures in the general population, delineate common mechanisms among them, and shed light on their relationship with other human organ systems[14,19,20]. To do this, we capitalized on nine imaging biomarkers recently derived from regional gray matter (GM) volumetrics derived from several large-scale disease-focused consortia, including ADNI[21] for Alzheimer's disease (AD1-2[12]), ABIDE[22] for autism spectrum disorder (ASD1-3[1]), LLD for late-life depression older than 60 years old (LLD1-2[2]), and PHENOM[23] for schizophrenia (SCZ1-2[23]). Using semi-supervised clustering and representation learning methodologies[24], we obtained nine imaging biomarkers capturing the neuroanatomical diversity across the four distinct brain diseases. AD1 and AD2 illustrate distinct atrophy patterns in the overall brain and medial temporal lobe, respectively[12]. ASD1, ASD2, and ASD3 showcase reduced overall volume, expanded subcortical volume, and increased cortical volume[1]. LLD1 and LLD2[2] exhibit augmented subcortical volume and overall brain atrophy, respectively. Finally, SCZ1 and SCZ2[23] display global brain atrophy and expanded basal ganglia volume. We first conceptualized these biomarkers as the dimensional neuroimaging endophenotypes (DNE), seeking to test the endophenotype hypothesis in psychiatry[25–27], which suggests that such

3

97   measurable intermediate biomarkers (i.e., the endophenotypes) bridge genetics and clinical
98   symptoms and the onset of the disease. They are thought to be more closely related to the
99   underlying etiology and genetics than the complex clinical symptoms or the disease itself.
100   Furthermore, the concept of dimensional representation reinforces the idea that diseases like AD
101   progress along a continuous spectrum. As such, categorizing disease heterogeneity into distinct
102   subtypes overlooks the presence of co-existing patterns within the same individuals (refer to
103   **Supplementary Method 1a** for details).
104   We evaluated the manifestation of the nine DNEs in the general population using the
105   neuroimaging and genetic data available in the UK Biobank study[28] (UKBB). The four pre-
106   trained disease-specific AI models were applied to the 39,178 UKBB participants with both brain
107   MRI[29] and genetic[30] data. To delineate the phenotypic landscape of the nine DNEs, we first
108   tested whether the neuroanatomical patterns of the nine DNEs are present in the UKBB general
109   population. Subsequently, we conducted a phenome-wide association study (PWAS) to establish
110   associations between the nine DNEs and 611 UKBB phenotypes, including brain imaging-
111   derived phenotypes (IDPs), traits related to multiple human organ systems, cognition, and
112   lifestyle factors. We performed a genome-wide association study (GWAS) linking the nine
113   DNEs to 6,477,810 quality-checked common single nucleotide polymorphisms (SNPs) to depict
114   their genetic architecture. Furthermore, we conducted analyses to investigate genetic
115   correlations, colocalization, and causal relationships between the nine DNEs, nine human organ
116   systems[17], and several chronic diseases. Finally, we assessed the ability of the nine DNEs and
117   their corresponding polygenic risk score (PRS) to predict 14 systemic disease categories, 8
118   cognitive scores, and mortality.
119

120   **Results**

121   Our analytic framework involves computational genomics, statistical methods, and machine
122   learning to elucidate the phenotypic landscape and genetic architecture of the nine DNEs, as
123   illustrated in **Fig. 1**.
124

4

All nine DNEs are evident in the general population

We tested whether the neuroanatomical patterns defined in the four disease populations could be found in the general population. We applied the DNE models pre-trained for each disease population to the UKBB general population to measure the degree of expression of each DNE at the individual level. The imaging data from the four disease populations and the UKBB general population were first statistically harmonized via the iSTAGING consortium[31] and then linearly corrected in the AI models for common confounders like demographics to alleviate potential domain shifts[32] (**Supplementary Text 1**).

We first summarize the neuroanatomical patterns of the nine DNEs (**Fig. 2a**). Overall, the original patterns identified in the disease populations[12,2,1,13] manifest in the general population. AD1 exhibits a pattern of brain atrophy (i.e., negative correlation) across various brain volumes, while AD2 involves focal atrophy of the medial temporal lobe. ASD1 captures a pattern of lower GM volumes in several subcortical regions, including the pallidum, amygdala, and putamen, whereas ASD2 reflects a pattern of relatively larger GM volumes (i.e., positive correlation) in subcortical regions. ASD3, conversely, is characterized by relatively larger GM volumes in several cortical areas, including the insula. LLD1 (positive correlation) and LLD2 (negative correlation) are characterized by concomitant patterns of regional GM volumes, prominently involving the middle frontal gyrus, the insula, and the thalamus. For schizophrenia, a widespread pattern of reduced brain volumes (e.g., insula) is associated with SCZ1, whereas SCZ2 displays increased volumes of the putamen and pallidum. The details of the P-value, sample sizes, and β values of the linear regression are presented in **Supplementary File 1** and **2**.

The nine DNEs showed different strengths of expression in the general population relative to what is seen in the disease populations from which they were derived. These differences were statistically significant except for ASD2, after correcting for multiple comparisons using the Bonferroni method (**Fig. 2b**). For instance, AD1, characterized by diffuse brain atrophy in the ADNI data, showed a significant under-expression (i.e., a smaller mean of the DNE score) in the general population. Conversely, the subcortical atrophy pattern originally identified in ASD1 from the ABIDE data displayed a significant over-expression (i.e., a larger mean of the DNE score) in the participants from the general population.

We then tested whether the nine DNEs differed between the healthy control and disease groups (AD, ASD, LLD, and SCZ) in the general UKBB population. Compared to the healthy control group (N=6390), a small proportion of patients with the four brain diseases showed significant differences (two-sample t-test) for AD1-2 (N=23), LLD1-2 (N=1329), and SCZ1-2 (N=23), except for ASD1-3 (only 6 ASD patients in this population). For example, AD2, characterized by focal medial temporal lobe atrophy, had a significantly lower mean of DNE in the healthy control (0.29±0.19) compared to the AD patient groups (0.45±0.27; P-value=1.1x10^{-4}). Detailed statistics for all nine DNEs are presented in **Supplementary Table 1**.

These results proved that the nine DNEs manifest in the general population and convey disease-specific information about the four brain diseases. The contrast in their expression (i.e., over- and under-expression) between the disease-specific and UKBB general populations is expected and underscores their potential relevance as sub-clinical or vulnerability quantitative indices.

The nine DNEs exhibit phenotypic associations with traits beyond the brain

169   To delineate their phenotypic landscape, we associated the nine DNEs with 611 phenotypes in
170   UKBB. To avoid circularity, the PWAS did not include the 119 GM ROIs derived from T1-
171   weighted MRI, from which the nine DNEs were derived. Out of the 611 additional clinical traits
172   spanning multiple organ systems, cognition, and lifestyle factors, we discovered 1818 significant
173   associations after applying the Bonferroni correction (P-value < 0.5/611) (**Fig. 2c**,
174   **Supplementary File 3**).
175   Of the 1818 significant associations, 91% were related to the brain. For example, the
176   mean intracellular volume fraction in the superior frontal-occipital fasciculus derived from the
177   multi-shell NODDI[33] model was significantly associated with AD1 [β=-0.67±0.02, -log$_{10}$(P-
178   value) > 300]. Multiple DNEs were significantly associated with the biological age gap (BAG:
179   AI-predicted age minus chronological age) of the brain [e.g., SCZ2: β=0.19±0.01, -log$_{10}$(P-
180   value)=50.10]. Furthermore, 2% of the phenotypes related to the musculoskeletal system were
181   associated with the nine DNEs. The nine DNEs were also largely associated with many
182   phenotypes related to mental health (1%). For example, the neuroticism score was significantly
183   associated with LLD2 [β=-1.09x10^{-2}±2.42x10^{-3}, -log$_{10}$(P-value)=5.20] (**Supplementary File 3**).
184   A previous study suggests distinct neural mechanisms between older individuals with neurotic
185   and non-neurotic depression, indicating diverse biological pathologies contributing to varying
186   clinical presentations of LLD[34].
187   We conducted two sensitivity analyses to validate the main PWAS results. We obtained
188   high concordance rates in split-sample (98.03%) and sex-stratified analyses (93.98%). Detailed
189   results can be found in **Supplementary Text 2** and **Supplementary File 4** and **5** for split-sample
190   and sex-stratified analyses.
191   As anticipated, 91% of the significant associations were linked to the brain, given that the
192   DNEs were derived from regional brain volumetrics in brain disease-specific populations.
193   However, it is noteworthy that these phenotypic associations extended beyond the brain,
194   providing evidence for the significant associations between the brain and other organ systems.
195   This brain-body connection was consistent with previous literature on multi-organ research using
196   imaging and genetic data[17,35,36].

6

Genome-wide associations identify 66 genomic loci

At the genome-wide significance level (P-value<$5x10^{-8}$), GWAS using PLINK for a linear regression model identified 10, 8, 5, 21, 9, 1, 3, 3, and 6 genomic loci significantly associated with AD1, AD2, ASD1, ASD2, ASD3, LLD1, LLD2, SCZ1, and SCZ2, respectively (66 in total, **Fig. 3a,** and **Supplementary File 6**). At a more stringent significance level (P-value<$5x10^{-8}/9$), 31 loci passed the Bonferroni correction, as annotated in **Fig. 3a** (query date: 2nd June 2023, via FUMA version: v1.5.4). To support the robustness of our GWAS, we estimated the intercept of linkage disequilibrium score regression (LDSC)[37] and obtained intercepts of 0.9997±0.0093, 1.0325±0.0091, 0.9962±0.0095, 1.0172±0.0099, 1.0117±0.0085, 1.0135±0.008, 1.0162±0.0094, 1.0101±0.0087, and 1.0124±0.0095 for the nine DNEs. All intercepts were close to 1, indicating no substantial genomic inflation in our GWASs. The Manhattan and QQ plots of the nine GWASs are presented in **Supplementary Figure 1-9** and are also publicly available on the MEDICINE knowledge portal: https://labs-laboratory.com/medicine/.

All DNEs are significantly heritable ($0.24<h^2<0.66$, P-value<$1x10^{-10}$) after Bonferroni correction (**Fig. 3a**, **Supplementary Table 2**). We employed the GCTA[38] software to estimate h^2, acknowledging that previous research has demonstrated variations in the magnitude of h^2 estimates based on the choice of methods. The h^2 estimates obtained through GCTA or similar methods may underestimate SNP-based heritability (i.e., missing heritability), potentially due to unaccounted factors such as gene-environment interactions, epistasis, and rare variant effects.

We further investigated the significant genomic loci by mapping them to protein-encoding genes and examining their functional implications through expression quantitative trait loci (eQTL) mapping. **Supplementary Figure 10** presents the regional Manhattan plot for the most significant genomic locus associated with each DNE. For example, we identified a locus associated with ASD2 (top lead SNP: rs3068507 at 20q11.21) and a neighboring locus associated with SCZ1 (top lead SNP: rs6088962 at 20q11.21), both of which mapped to the *MYLK2* gene (**Supplementary Figure 10d** and **h**). The *MYLK2* gene encodes a myosin light chain kinase primarily expressed in adult skeletal muscle.

We conducted seven sensitivity analyses to validate the main GWAS results. We obtained perfect concordant rates (100%) and similar genomic inflation factors using fastGWA[39,40] for a generalized linear mixed model in the nine GWAS. Specifically, we excluded the related individuals (up to 2nd-degree) in our genetic quality check pipeline; mixed effect models like fastGWA can detect additional genetic relatedness without excluding individuals by using a sparse genomic relationship matrix, significantly reducing the computational burden for large-scale GWAS. This sensitivity check further supports that no substantial genomic inflation exists in our main GWASs. We also observed high concordance rates in split-sample, sex-stratified (63.26-92.54%), and longitudinal GWAS analyses (100%, *N*=1116), but the concordance rates were relatively low in non-European ancestry GWAS, independent ADNI whole-genome sequencing GWAS, and six case-control GWAS[41–46] of neurodegenerative and neuropsychiatric disorders from the Psychiatric Genomics Consortium (PGC)[47] (**Supplementary Table 3a**). The sample sizes for the non-European (*N*=4783) and ADNI (*N*=1555) samples are small; the case-control GWAS from the PGC may overlook the heterogeneity within each disease. Detailed results are presented in **Supplementary Text 3** for the sensitivity results, **Supplementary File 7-13** for replicated SNPs/loci, and **Supplementary Figure 1-9** for Manhattan and QQ plots and the LDSC intercepts.

The genetic associations of the nine DNEs parallel their phenotypic associations

243 We performed a phenome-wide look-up analysis to understand the phenotypic associations in the
244 literature for the identified genomic loci in our GWAS.
245   In total, 2525 clinical traits were associated with genetic variants in our GWAS,
246 including traits linked to multiple organ systems, cognition, and lifestyle factors (**Fig. 3b** and
247 **Supplementary File 14**). The genomic loci were largely associated with clinical traits of the
248 brain (53%), musculoskeletal (17%), immune system (6%), neurodegenerative (1%), and
249 neuropsychiatric (1%) diseases. For example, AD2 genomic loci were largely associated with
250 traits related to the brain (565 out of 781, e.g., brain IDPs), musculoskeletal (133/781, e.g.,
251 standing height), immune (17/781, e.g., reticulocyte count), cognition (15/781, e.g., cognitive
252 performance), lifestyle factors (13/781, e.g., smoking), and neurodegenerative traits (1/781, i.e.,
253 neurofibrillary tangles).
254   The findings closely align with the phenotypic associations observed in **Fig. 2c**,
255 reinforcing that the DNEs share genetic determinants linked to organs beyond the brain, lifestyle
256 factors, and cognition.

8

The genetic correlation of the nine DNEs

To understand the shared genetic underpinnings, we estimated the genetic correlation[37] (g_c) between the nine DNEs, the BAG of nine human organ systems[17], and six brain diseases (AD, attention-deficit/hyperactivity disorder, autism spectrum disorder, bipolar, obsessive-compulsive disorder, schizophrenia; **Supplementary Table 3a**) from PGC and four lifestyle factors and cognitive scores (**Supplementary Table 3b**).

We first estimated the g_c between each pair of DNEs (**Fig. 4a**). Numerous DNEs exhibited strong genetic correlations among each other. The highest positive genetic correlation was obtained between ASD2 and SCZ1 (g_c=0.57±0.04); the highest negative genetic correlations were obtained between ASD2 and ASD1 (g_c=-0.55±0.04), and between ASD3 and SCZ1 (g_c=-0.51±0.05). We also observed a substantial alignment between the phenotypic correlation (p_c) and the genetic correlation of pairwise DNEs, supporting the long-standing Cheverud's Conjecture[48]. However, we identified two exceptions where the observed phenotypic and genetic correlations exhibited opposite directions. ASD1 and ASD3 showed a negative phenotypic (p_c=-0.39±0.08) but a positive genetic correlation (g_c=0.21±0.05); ASD1 and LLD1 showed a negative phenotypic (p_c=-0.34±0.09) but a positive genetic correlation (g_c=0.16±0.07) (**Supplementary Table 4**). This implies that non-genetic factors, such as lifestyle and environmental factors, may exert opposite influences on the two DNEs. We performed additional MAGMA gene-set analysis[49] to test the genetic similarity between ASD2 and SCZ1. The most significant biological pathway underlying ASD2 is the negative regulation of locomotion (GO 0040013, P-value=2.27x10^{-5}, β=0.22±0.02), implicated in biological processes that stop, prevent, or reduce the frequency, rate, or extent of locomotion of a cell or organism. The most significant biological pathway for SCZ1 is the negative regulation of neurotransmitter transport (GO 0051589, P-value=1.41x10^{-5}, β=0.22±0.02), involved in biological processes that downregulate the directed movement of a neurotransmitter into, out of, or within a cell. In particular, the latter supports the involvement of dopamine and glutamate, two major neurotransmitters in the central nervous system, in schizophrenia[50].

Between the nine DNEs and the BAGs across nine human organ systems, we found significant genetic correlations between AD1 (g_c=0.23±0.05), ASD1 (g_c=0.44±0.05), LLD2 (g_c=0.24±0.07), SCZ1 (g_c=0.26±0.06), and the brain BAG, and between ASD1 and the eye BAG (g_c=0.19±0.07) (**Fig. 4b** and **Supplementary Table 5**).

Finally, we also found a marginally significant genetic correlation between AD2 and AD (g_c=0.22±0.12), AD1 and bipolar disorder (BIP, g_c=-0.08±0.04), and ASD3 and BIP (g_c=0.09±0.04) using GWAS summary statistics from PGC (**Fig. 4c** and **Supplementary Table 6a**). We observed a nominal genetic correlation signal between ASD1 and reaction time (g_c=0.35±0.15; **Fig. 4d** and **Supplementary Table 6b**).

In summary, the nine DNEs demonstrate substantial genetic correlations among themselves and with organ systems beyond the brain. These findings highlight the interconnectedness of the neuroanatomical patterns and genetic determinants across multiple body systems and diseases, suggesting shared underlying disease mechanisms and potential pleiotropic effects.

The genetic colocalization of the nine DNEs

9

300   To seek the shared causal variants between two clinical traits (e.g., AD1 vs. LLD2), we
301   performed Approximate Bayes Factor colocalization[51] analyses between the nine DNEs (**Fig.**
302   **4e**), with the nine BAGs (**Fig. 4f**), and the six brain disorders from PGC[47] (**Fig. 4g**).
303   Among the nine DNEs, we detected 44 causal variants (SNPs) exhibiting significant
304   colocalization signals. We showcased the shared causal variant (rs2790099 at 6p21.1) between
305   ASD2 and SCZ2 with a PP.H4.ABF (Approximate Bayes Factor)=0.92 (**Fig. 4e**), which
306   examines the posterior probability (PP) to evaluate the hypothesis, the presence of a single
307   shared causal variant associated with both traits within a specific genomic locus. This causal
308   SNP was mapped to the *RUNX2* gene. The loss of function in *RUNX2* causes a rare autosomal
309   dominant skeletal disorder – cleidocranial dysplasia[52], but it was implicated in ASD or SCZ in
310   previous literature.
311   Between the nine DNEs and nine BAGs, we identified 13 causal variants (SNPs)
312   exhibiting significant colocalization signals. We showcased the shared causal variant (rs5848503
313   at 3p22.1) between ASD2 and the brain BAG with a PP.H4.ABF=0.95 (**Fig. 4f**). One mapped
314   gene in this locus is the *MOPB* gene, which encodes the myelin-associated oligodendrocytes
315   basic protein and is actively involved in the structural constituent of the myelin sheath and
316   nervous system development. This gene was previously implicated in ASD using single-cell
317   genomics[53], SCZ[54], amyotrophic lateral sclerosis, and Parkinson's disease[55].
318   Between the nine DNEs and six brain diseases from PGC, we identified 6 causal variants
319   (SNPs) exhibiting significant colocalization signals. We showcased the shared causal variant
320   (rs9257566 at 6p22.1) between ASD3 and SCZ with a PP.H4.ABF=0.82 (**Fig. 4g**). In this locus,
321   multiple olfactory receptor (OR) genes and the dysfunction of the olfactory system were
322   implicated in SCZ[56,57] and ASD[58,59]. For instance, the *OR2J2* and *OR2J3* genes are two protein-
323   coding genes in copy number variants associated with SCZ using microRNA data[60]. The causal
324   SNP (rs9257566) was associated with SCZ and brain IDP, such as white matter microstructural
325   measures (**Supplementary Figure 11**). Besides those two conditions, AD has also been widely
326   associated with early olfactory dysfunction[61,62]. The sensitivity checks on the prior probability
327   (*p12*) for the three illustrations are shown in **Supplementary Figure 12a-c**. The causal variant,
328   cytogenetic region, and their colocation signal direction (based on β coefficients) are presented in
329   **Supplementary Figure 13a-c**. Detailed results are shown in **Supplementary File 15-17**.
330   The genetic colocalization of the nine DNEs revealed causal genetic variants, indicating
331   that the same genomic regions may causally influence the expression of these AI-derived
332   endophenotypes.
333

334   **The causal relationship of the nine DNEs**

335   We applied bidirectional two-sample Mendelian randomization analyses[63] to depict a causal
336   network between the nine DNEs, the eight BAGs (excluding the brain BAG), and eleven chronic
337   diseases spanning the whole-body system.
338   For each pair of DNEs, as the GWAS populations completely overlapped, conducting
339   two-sample Mendelian randomization was not feasible[64]. Alternatively, the split-sample GWAS
340   did not yield sufficient statistical power due to the limited number of instrumental variables (VI)
341   available (< 6 SNPs).
342   Among the nine DNEs and eight BAGs, we found potential causal effects of the eye
343   BAG on LLD1 [P-value=4.57×10^{-3}, OR (95% CI) = 1.14 (1.04, 1.24), number of SNPs=16], the
344   cardiovascular BAG on ASD3 [P-value=6.04×10^{-3}, OR (95% CI) = 1.16 (1.04, 1.29), number of
345   SNPs=34], and the pulmonary BAG on LLD2 [P-value=1.98×10^{-3}, OR (95% CI) = 1.14 (1.04,

10

346   1.25), number of SNPs=49]. No significant causal signals persisted after the Benjamini-
347   Hochberg correction in the inverse analyses (**Fig. 4h**). Details of the results, including all five
348   different Mendelian randomization estimators, are shown in **Supplementary File 18**.
349   Between the nine DNEs and eleven chronic diseases, encompassing brain-related
350   conditions and diseases affecting other organs, we identified a potential causal effect from AD2
351   to AD using the GWAS summary statistics from PGC – the largest sample size (N=1,126,536
352   individuals) in the AD case-control study [P-value=1.74×10^{-4}, OR (95% CI) = 1.25 (1.11, 1.40),
353   number of SNPs=7] (**Fig. 4i**). We didn't detect a causal link in the opposite direction from AD to
354   AD2. This aligns with the endophenotype hypothesis, suggesting that DNEs are situated within
355   the causal pathway from genetics to external phenotypes, such as AD diagnosis and cognitive
356   decline. Details of the results, including all five different Mendelian randomization estimators,
357   are shown in **Supplementary File 19**. The results of the sensitivity check are presented in
358   **Supplementary Figure 14-17**.
359   The Mendelian randomization results further emphasize the potential benefits of overall
360   organ health for brain-related conditions. This highlights the interconnectedness between various
361   organ systems and the brain, underscoring the significance of a holistic health and disease
362   prevention approach.

The nine DNEs predict14 systemic diseases and mortality

We investigated the added prediction power of the nine DNEs and their respective PRS for 14 systemic diseases based on the ICD-10 code (**Supplementary Table 7-8**), 8 cognitive scores(**Supplementary Table 9**), and mortality outcomes (i.e., the date of death). Of note, we did not perform prediction on the four brain diseases (AD, ASD, LLD, and SCZ) due to the small and highly imbalanced sample sizes in the UKBB general population. As anticipated, the prediction performance across all tasks was modest, considering that the DNEs were derived from specific disease populations.

In addition to commonly available features, such as age and sex, we found that AD1, ASD1, LLD1, SCZ1, and SCZ2 provided additional prediction power (i.e., incremental R^2) for many disease categories. Across the 14 disease categories, the DNEs showed higher incremental R^2 in mental and behavioral disorders (ICD-10 code: F group) and diseases linked to the central nervous system (ICD-10 code: G group) than other disease categories, proving that the nine DNEs in the general population capture disease-related effects of the four brain diseases. Combining all nine DNEs further improved the incremental R^2, especially in mental and behavioral disorders (R^2=1.01%, P-value=1.74×10^{-5}) and diseases linked to the central nervous system (R^2=0.63%, P-value=1.33×10^{-5}) (**Fig. 5a**). The incremental R^2 values for all tests are shown in **Supplementary Table 7**. All metrics, encompassing sample sizes and incremental R2 for both the null and alternative models, are outlined in **Supplementary File 20**. Results using only the PRS target population are presented in **Supplementary Figure 18**.

Compared to the nine DNEs, the nine PRSs provided smaller additional prediction power. For example, the PRS for ASD3 explained an additional 0.05% of the variance (incremental R^2) in diseases associated with the blood and immune systems (P-value=0.03), as well as neoplasms (P-value=0.04). Combining all nine PRSs improves the incremental R^2, particularly in mental and behavioral disorders (R^2=0.3%, P-value=0.047). No results survived multiple comparisons using the Benjamini-Hochberg method (**Fig. 5b**). Detailed results are shown in **Supplementary Table 8** and **File 21**.

We assessed the prediction ability of support vector machines (SVM) at the individual level to classify the 14 disease categories. The highest performance was observed for eye diseases (ICD-codes: H0-5). Age and sex significantly enhanced the classification accuracy. Including age and sex alongside the 9 DNEs and 9 PRSs boosted the classification accuracy from 0.55 to 0.65. The inclusion of PRSs, DNEs, and the combination of both, along with age and sex as features, resulted in improved classification accuracy for mental and behavioral disorders. For example, the accuracy increased from 0.51 to 0.55 and 0.57 for features of age and sex, 9 DNEs, and 9 PRSs, incrementally (**Fig. 5c**). These findings highlight the added value of incorporating the nine DNEs and PRSs in predicting these disease categories. Detailed results are shown in **Supplementary Table 9a**. The full evaluation metrics of the cross-validated and independent test results are presented in **Supplementary File 22**.

We examined the predictive capability of these feature sets in estimating 8 cognitive scores. The digit symbol substitution test (DSST) demonstrated the highest performance, reaching a Pearson's r of 0.46 (e.g., P-value=3.9×10^{-189} and MAE=3.75 for the feature set of 9 DNE plus covariates) in the independent test dataset using all different sets of features (**Fig. 5d**). The combination of DNEs and PRSs did not notably enhance prediction accuracy. However, contrary to the 14 systemic disease classifications, incorporating the 119 GM imaging-derived phenotypes alongside DNEs and PRSs resulted in a 2% increase in the prediction accuracy for fluid intelligence, measured by Pearson's r (**Supplementary Table 9b**). The full evaluation

12

409   metrics of the cross-validated and independent test results are presented in **Supplementary File**
410   **23.**
411   Finally, we evaluated the prediction power of the nine DNEs and PRSs for mortality risk
412   prediction using the Cox regression. Among these, SCZ1, SCZ1-PRS, ASD1, and AD1-PRS
413   were significantly associated with the risk of mortality (**Fig. 5e** and **Supplementary Table 10a**).
414   Adding SCZ1, AD1-PRS, ASD1, and SCZ1-PRS to age and sex further improved the prediction,
415   but the performance decreased afterward (**Fig. 5f**). Lastly, incorporating the nine DNEs from the
416   second scan of 1348 participants into the model slightly increased the statistical significance and
417   the HR (**Supplementary Table 10b** and **c**).

13

Discussion

This study investigated the manifestation of nine disease-related brain endophenotypes – derived from four case-control studies via semi-supervised AI methods – in the general population of 39,178 participants in UKBB. We assessed commonalities and differences among the nine DNEs, their genetic correlates in the general population, their relationships with the multiple human organ systems, and their predictive capacity for 14 systemic disease categories and mortality. Our findings demonstrate the potential of the nine AI-derived DNEs in identifying high-risk individuals within the general population prone to developing the four major brain disorders.

Shared neuroanatomical patterns and genetic determinants

Understanding the shared disease mechanism of neurodegenerative and neuropsychiatric diseases is a complex and ongoing challenge in medical research[15,16,41,43–46,65]. Our results suggest that shared underlying mechanisms and genetic factors may contribute to the development and progression of these disorders. This notion of shared disease mechanisms across the four major neurodegenerative and neuropsychiatric diseases, namely ASD, SCZ, LLD, and AD, has garnered considerable attention and reshaped our understanding of these conditions[15,16].

Despite the inherent heterogeneity among neuroanatomical patterns observed in different brain diseases (**Fig. 2a**), a notable commonality exists regarding their manifestations, which might emanate from underlying mechanisms sharing neuropathologic characteristics and pathways. As an illustration, AD1, LLD2, and SCZ1 exhibited a negative correlation (brain atrophy) with widespread cortical volumes, such as the bilateral insula and middle frontal gyrus. This aligns with expectations, considering that the UKBB population includes individuals primarily from mid to late life (above 45 years). From an etiological standpoint, various factors can contribute to the global cortical volume reduction within the general population, with late-onset neurodegenerative and neuropsychiatric disorders and aging exerting a significant impact. Likewise, ASD2 and SCZ2 exhibited a positive association with the basal ganglia, including the globus pallidum. This could imply the existence of potential protective genetic or environmental factors that collectively contribute to the concept of "brain reserve", which might mitigate volume loss in a portion of the general population. Notably, we previously revealed that individuals predominantly expressing SCZ2 exhibited higher levels of education[23] and higher remission rates than those primarily influenced by SCZ1. Alternatively, these volume increases might reflect neuropathologic mechanisms, such as disrupted connectivity, which are not necessarily associated with neurodegenerative and neurodevelopmental components related to relatively lower brain volumes. Ultimately, another significant aspect to consider involves the impact of medications prescribed by clinicians, affecting both disease-specific and general populations. Research indicates that antipsychotic medications, commonly prescribed for most individuals with schizophrenia and some with ASD and AD, have been shown to delay brain volume loss in the basal ganglia[66] and pallidum[67].

The commonalities in neuroanatomical patterns across brain diseases can be attributed to several factors. First, shared genetic factors may influence brain structure and function[30,31], contributing to similar neuroanatomical alterations across different diseases. Genetically, this was largely evidenced by our genetic correlation (**Fig. 4a**) and colocalization results (**Fig. 4e**). For instance, ASD2 showed prominent positive genetic overlap with SCZ1. Historically, there

14

463 has been a long-standing association between ASD and SCZ, leading to the notion that autism
464 could be a form of "childhood schizophrenia"[68]. This conceptual link between the two conditions
465 has been debated and discussed. Previous case-control neuroimaging studies demonstrated
466 divergent structural and functional brain patterns in individuals with ASD compared to those
467 with SCZ[69,70], largely ignoring the neuroanatomical heterogeneity within each condition. Genetic
468 variants that impact key signaling pathways, synaptic function, and neuronal connectivity[71,72]
469 could influence multiple disease phenotypes, leading to overlapping neuroanatomical patterns.
470   AD1 also shared genetic similarities with LLD1, both characterized by spatially extensive
471 brain atrophy and increased brain age. Previous studies found a higher prevalence of depressive
472 symptoms and LLD in individuals with AD compared to the general population[73–75]. The
473 relationship between AD and LLD likely involves multiple factors and may be bidirectional. On
474 the one hand, LLD may increase the risk of developing AD or accelerate the progression of
475 cognitive decline in individuals already affected by AD. On the other hand, AD-related changes
476 in the brain, such as neuroinflammation and neurochemical imbalances, may worsen depressive
477 symptoms in individuals with LLD.
478   Recognizing the shared disease mechanisms across the four brain diseases underscores
479 the importance of a broader perspective on clinical presentations and underlying biological
480 mechanisms. This understanding is important for developing targeted and personalized
481 approaches to patient care, leading to more effective treatments and interventions. Future
482 research may explore disease heterogeneity to transcend traditional classification boundaries and
483 identify data-driven subtypes or dimensions within a transdiagnostic framework[76].
484
485 **Beyond the brain**

486 Our findings strongly concur with a paradigm shift in treating brain diseases. While the
487 conventional approach has predominantly concentrated on interventions targeting the brain,
488 emerging evidence highlights the critical importance of considering the broader systemic and
489 environmental factors that influence disease onset and progression.
490   Unraveling the intricate interconnections between the brain and other organ systems is
491 crucial in broadening our understanding of brain diseases, as demonstrated by our findings and
492 other findings. The brain does not function in isolation but interacts with and is influenced by
493 various physiological systems throughout the body. Our results showed a close genetic
494 association and causality between the DNEs and the eye, cardiovascular, and pulmonary systems
495 (**Fig. 4b**, **f**, and **h**). These findings parallel previous literature. For instance, eye-related
496 pathological changes have been revealed to mirror early signs of neurological and
497 neuropsychiatric conditions[77]. The nervous and cardiovascular systems – the heart-brain axis –
498 are intricately linked, with brain regions controlling heart function via sympathetic and
499 parasympathetic pathways[78]. Dysfunctions in one system can affect the other's function, resulting
500 in brain and cardiovascular diseases. The immune system plays a crucial role in modulating
501 inflammation and neuroinflammation, which are implicated in many brain disorders, such as
502 AD[79], SCZ[80], and depression[81]. Similarly, the gut-brain axis highlights the bidirectional
503 communication between the gut microbiota and the brain, with emerging evidence linking
504 alterations in the gut microbiome to brain diseases such as Parkinson's disease[82] and
505 depression[83]. Understanding and targeting these systemic interactions can modulate disease
506 processes and improve treatment outcomes.
507   Furthermore, considering environmental and lifestyle factors is essential in treating brain
508 diseases[84]. Our previous work[17] has shown that the BAGs of nine human organ systems comply

15

509 with Cheverud's Conjecture: the phenotypic correlation of two BAGs mirrors their genetic
510 correlations. However, herein we showed that the phenotypic correlation between two DNEs
511 (e.g., ASD1 vs. LLD1) did not reflect their underlying genetic correlation (**Fig. 4a**), indicating
512 potentially strong environmental and lifestyle factors that exert opposite effects on the two
513 DNEs. Furthermore, an interesting observation from our study was that the heritability estimate
514 (h^2) of early-onset diseases, such as ASD, was higher than that of late-onset diseases, such as
515 LLD, within the three neuropsychiatric disorders. This finding suggests that genetic factors play
516 a more prominent role in developing ASD at a younger age. In contrast, other factors, such as
517 environmental influences, socioeconomic factors, and lifestyle choices, may have a stronger
518 impact on developing LLD later in life. These differential heritability patterns shed light on the
519 complex interplay between genetic and non-genetic factors in the underlying disease mechanism
520 of neurodegenerative and neuropsychiatric disorders across different stages of life. These
521 heritability patterns aligned with a previous study that examined multiple GWAS drawn from
522 more than 200,000 patients for 25 brain-associated disorders and 17 phenotypes[16].
523   In conclusion, going beyond the brain is crucial for understanding and treating brain
524 diseases. By considering the connections between the brain and other organ systems,
525 understanding the impact of environmental and lifestyle factors, and harnessing the power of
526 advanced AI technologies, we can develop more effective and personalized approaches to
527 prevent, diagnose, and treat brain diseases.
528
529 **AI-derived DNEs for precision diagnostics**

530 The present study leverages cutting-edge, semi-supervised AI methods[24] and open science
531 advancements to enhance our understanding of disease heterogeneity in neurodegenerative and
532 neuropsychiatric disorders. In this context, implementing these AI-derived DNEs at early disease
533 or preclinical stages – in the general population – may facilitate the identification of individuals
534 at risk, and the initiation of proactive interventions before the onset of noticeable symptoms,
535 likely leading to more effective treatments and interventions and better outcomes.
536   The proposed AI-derived DNEs capture intricate brain structure and function variations,
537 often subtle and spatially complex, which traditional diagnostic methods and case-control studies
538 may overlook. By quantifying the neuroanatomical patterns associated with specific brain
539 disorders, DNEs may offer a personalized disease vulnerability assessment, inform interventions
540 at early preclinical stages, and potentially prevent or delay the onset of symptoms. At the
541 individual level, integrating genetic information (i.e., PRSs) with DNEs significantly improves
542 prediction performance for 14 systemic diseases and mortality outcomes (**Fig. 5**). In addition, our
543 Mendelian randomization analyses supported the well-established endophenotype hypothesis in
544 genetic psychiatry[25] – endophenotype in psychiatric disorders resides inside the causal pathway
545 from underlying genetics to their exo-phenotypes (i.e., the disease syndrome itself), thereby
546 being closer to its disease mechanisms. We found that AD2, characterized by focal medial
547 temporal lobe atrophy, exerted a causal relationship with AD. However, we did not find evidence
548 of a reverse causal relationship, suggesting that the underlying genetics may influence the
549 development of AD through the DNE, although it may not be the exclusive pathway contributing
550 to the disease. This highlights the role of genetics in influencing the disease process, particularly
551 through the identified DNE, shedding light on potential pathways and mechanisms involved in
552 AD development.
553
554 **Limitation**

16

555   The present study has several limitations. Firstly, the genetic analysis focused exclusively on
556   common genetic variants. Future investigations should explore the contribution of rare variants
557   to these brain diseases. Secondly, it is important to recognize that our GWAS analyses
558   predominantly involved participants of European ancestry, limiting the generalizability of the
559   genetic findings to other populations with different ancestral backgrounds. Further research
560   efforts are necessary to collect more diverse genetic data and include underrepresented racial and
561   ethnic groups to enhance the generalizability of the findings. Additionally, the validation of the
562   nine DNEs would benefit from additional longitudinal analyses. Fortunately, ongoing efforts to
563   collect longitudinal brain MRI data in UKBB[85] hold promise for providing valuable insights to
564   the scientific community and advancing the field of precision medicine. Furthermore, more
565   advanced methodological developments will be developed and integrated within our semi-
566   supervised clustering learning framework to alleviate potential domain shifts[86]. Finally, our
567   future research will incorporate multimodal imaging to generate DNEs sensitive to a broader
568   range of brain alterations, including macrostructural volumetric changes, functional disruptions,
569   and structural network abnormalities.
570

571   **Outlook**

572   Together, our AI-derived DNEs have emerged as novel instruments for precision medicine. By
573   capturing the complexity and heterogeneity of brain disorders, DNEs provide a better
574   understanding of disease pathology, facilitate personalized risk assessment, and hold promise for
575   targeted interventions and population selection.

17

Methods

Study populations

Our previous studies used semi-supervised AI models to define the nine DNEs from four disease case-control populations. These populations consisted of 865 healthy controls (CN), 1096 individuals with mild cognitive impairment (MCI), and 414 AD patients from ADNI[21] for AD1 and AD2, 362 typically developing controls, and 307 patients with autism spectrum disorder (ASD) from ABIDE[22] for ASD1-3, 495 healthy controls and 501 LLD patients from the LLD study[2] for LLD1-2, and 364 healthy controls and 307 SCZ patients from PHENOM[23] for SCZ1-2. For more detailed information about the characteristics of the study populations, please refer to the original papers.

The trained AI models were then applied to the UKBB general population as independent data. UKBB is a population-based study of approximately 500,000 people recruited from the United Kingdom between 2006 and 2010. The UKBB study has ethical approval, and the ethics committee is detailed here: https://www.ukbiobank.ac.uk/learn-more-about-uk-biobank/governance/ethics-advisory-committee. The protocols of this study were approved by the University of Pennsylvania institutional review board. The current study analyzed 39,178 multimodal brain MRI data from UKBB. T1-weighted MRI data were locally processed at the University of Pennsylvania; imaging-derived phenotypes (IDP) from diffusion and resting-state functional MRI were downloaded from UKBB. In addition, we processed the imputed genotype data[28] from UKBB for GWAS analyses. Last, other clinical traits were also analyzed, including phenotypes related to nine human organ systems. The current work was performed under application numbers 35148 and 60698. We detail our dataset splits in **Supplementary Text 4**.

Semi-supervised AI methods to derive the nine DNEs

The methodologies used in the current study to derive the nine DNEs belong to the semi-supervised learning algorithms (**Fig. 1a**) pioneered by our group. Refer to a review for details of this type of modeling. In particular, the current study employed the HYDRA[87] and Surreal-GAN[14] models.

(a): Surreal-GAN: Surreal-GAN[14] dissects underlying disease-related heterogeneity via a deep representation learning approach, instead of the discriminative SVM, under the principle of semi-supervised clustering – the "*1-to-k*" mapping. The methodological advance of this method is that Surreal-GAN models disease heterogeneity as a continuous dimensional representation, enforces monotone disease severity in each dimension, and allows the non-exclusive manifestation of all dimensions in the same participant (**Supplementary Method 1a**).

(b): HYDRA: HYDRA leverages a widely used discriminative method, i.e., support vector machines (SVM), to seek the "*1-to-k*" mapping. The novelty is that HYDRA extends multiple linear SVMs to the non-linear case piecewise, thereby simultaneously serving for classification and clustering. Specifically, it constructs a convex polytope by combining the hyperplane from *k* linear SVMs, separating the CN group from the *k* subpopulation of the PT (patient) group. Intuitively, each face of the convex polytope can be regarded to encode each subtype, capturing a distinct disease effect (**Supplementary Method 1b**). **Supplementary Text 5** details the original image patterns of the diseased population in our previous study.

18

620
621 **Imaging analyses**

622 **(a): T1-weighted MRI processing**: All images were first corrected for magnetic field intensity
623 inhomogeneity.[88] A deep learning-based skull stripping algorithm was applied to remove extra-
624 cranial material. In total, 145 IDPs were generated in gray matter (GM, 119 ROIs), white matter
625 (WM, 20 ROIs), and ventricles (6 ROIs) using a multi☐atlas label fusion method from the
626 MUSE atlas.[89] The ROIs were fit to the four machine learning models to derive the nine DNEs.
627 The imaging quality check is detailed in **Supplementary Method 2**.

628
629 **(b): Neuroanatomical pattern of the nine DNEs**: We assessed the neuroanatomical patterns
630 exhibited by the nine DNEs within the general population. Since the DNEs were defined based
631 on the 119 GM ROIs obtained from T1-weighted MRI scans, we aimed to test whether these
632 patterns observed in the disease populations were manifested in the general population. To this
633 end, we used a linear regression model in which each DNE was treated as the dependent
634 variable, while the ROI, age, age-squared, sex, age x sex interaction, age-squared x sex
635 interaction, intracranial volume, brain positions in the scanner (lateral, transverse, and
636 longitudinal; Field ID: 25756-25758), and head motion were considered independent variables
637 and covariates.

638
639 **(c): PWAS for the nine DNEs:** We performed PWAS to associate the nine DNEs to each of the
640 611 additional phenotypes. PWAS excluded the 119 GM ROIs utilized to derive the nine DNEs
641 to prevent any potential circular effects. Instead, the analysis incorporated IDPs from other
642 modalities, such as diffusion and resting-state functional MRI. The same linear regression
643 models and multiple comparison corrections were employed.
644 To check the robustness of our PWAS results, we also performed two sensitivity checks:
645 *i*) sex-stratified PWAS for males and females, and *ii*) split-sample PWAS by randomly dividing
646 the entire population into two splits (sex and age did not significantly differ).

647
648 **Genetic analyses**

649 We used the imputed genotype data for all genetic analyses, and our quality check pipeline
650 resulted in 31,929 participants with European ancestry and 6,477,810 SNPs. First, we excluded
651 36,394 related individuals (up to 2nd-degree) from the full UKBB sample (*N*~500k) using the
652 KING software for family relationship inference[90]. We then removed duplicated variants from all
653 22 autosomal chromosomes. Individuals whose genetically identified sex did not match their
654 self-acknowledged sex were removed. Other excluding criteria were: i) individuals with more
655 than 3% of missing genotypes; ii) variants with minor allele frequency (MAF) of less than 1%;
656 iii) variants with larger than 3% missing genotyping rate; iv) variants that failed the Hardy-
657 Weinberg test at 1×10^{-10}. The Hardy-Weinberg test removes the SNPs that deviate from the
658 expected HWE frequency, ensures the integrity of the genetic data, reduces false-positive
659 findings, and improves the overall robustness of the GWAS results. To adjust for population
660 stratification,[91] we derived the first 40 genetic principle components (PC) using the FlashPCA
661 software[92]. Details of the genetic quality check protocol are described elsewhere.

662
663 **(a): GWAS**: For GWAS, we ran a linear regression using Plink[93] for each DNE, controlling for
664 confounders of age, age-squared, sex, age x sex interaction, age-squared x sex interaction, the

19

665 first 40 genetic principal components, total intracranial volume, three brain position parameters
666 in the scanner, and head motion were included, as suggested by a previous study[30]. We adopted
667 the genome-wide P-value threshold (5×10^{-8}) and annotated independent genetic signals
668 considering linkage disequilibrium (see below).
669 To check the robustness of our GWAS results, we also performed several sensitivity
670 checks: *i*) fastGWA[39,40] for a generalized mix effect model, *ii*) sex-stratified GWAS for males
671 and females, *iii*) split-sample GWAS by randomly dividing the entire population into two splits
672 (sex and age did not significantly differ), *iv*) comparison of the GWAS results using the 1348
673 participants (i.e., 1116 European ancestry) that were collected for baseline and longitudinal scans
674 from UKBB, *v*) non-European GWAS (*N*=4783), *vi*) independent GWAS on ADNI whole-
675 genome sequencing data (*N*=1555) on AD1 and AD2, *vii*) concordance with six European
676 ancestry GWAS from PGC, including AD, ADHD, ASD, BIP, OCD, and SCZ (**Supplementary
677 Table 3a**).
678
679 **(b): SNP-based heritability**: We estimated the SNP-based heritability (h^2) using GCTA[38] with
680 the same covariates as in GWAS. GCTA estimates the SNP-based heritability using a method
681 called restricted maximum likelihood (REML) to quantify the proportion of phenotypic variance
682 in a trait that the additive effects of all common SNPs can explain, which was claimed to address
683 the "missing heritability". The main steps involved in GCTA include constructing the genetic
684 relationship matrix, modeling phenotypic variance, and using REML to estimate the h^2.
685
686 **(c): Annotation of genomic loci**: The annotation of genomic loci and mapped genes was
687 performed via FUMA[94]. For the annotation of genomic loci, FUMA first defined lead SNPs
688 (correlation $r^2 \leq 0.1$, distance < 250 kilobases) and assigned them to a genomic locus (non-
689 overlapping); the lead SNP with the lowest P-value (i.e., the top lead SNP) was used to represent
690 the genomic locus. For gene mappings, three different strategies were considered. First,
691 positional mapping assigns the SNP to its physically nearby genes (a 10 kb window by default).
692 Second, eQTL mapping annotates SNPs to genes based on eQTL associations using the GTEx v8
693 data[95]. Finally, chromatin interaction mapping annotates SNPs to genes when there is a
694 significant chromatin interaction between the disease-associated regions and nearby or distant
695 genes[94]. The definition of top lead SNP, lead SNP, independent significant SNP, and candidate
696 SNP can be found in **Supplementary Method 3**.
697 To determine if a genomic locus is new (i.e., newly discovered in our study), we used
698 FUMA to query the candidate SNPs, independent significant SNPs, and top lead SNP in the
699 EMBL-EBI GWAS Catalog, taking LD into account. For these new loci, we further manually
700 queried the non-significant SNPs in LD (r^2>0.1) with these SNPs directly on the GWAS Catalog
701 platform on 29th October 2024. A locus is considered new if no previous GWAS has identified
702 associations with any of these SNPs. It is worth noting that the current definition of new loci is
703 not completely exhaustive and objective, as new GWAS data are being collated into the GWAS
704 Catalog, while other public data platforms (such as the GWAS Catalog and the IEU Open
705 GWAS Project) are not considered.
706
707 **(d): Phenome-wide association queries for the identified loci in the GWAS Catalog**: We
708 queried the candidate and significant independent SNPs, considering LD (**Supplementary
709 Method 3**), within each locus in the EMBL-EBI GWAS Catalog (query date: 2nd June 2023 and
710 also via FUMA version: v1.5.4) to determine their previously identified associations with any

20

711   other traits. For these associated traits, we further mapped them into several high-level categories
712   for visualization purposes. We categorized these traits based on their primary affected organ
713   systems, with examples including blood pressure under cardiovascular, brain MRI-derived
714   measures under brain, and AD under neurodegenerative disorders. Other platforms, such as the
715   GWAS Atlas (https://atlas.ctglab.nl/PheWAS), used a similar categorization approach; we
716   followed a similar approach to curating the high-level categories for the trait-category mapping.
717

718   **(e): Genetic correlation**: We used the LDSC[37] software to estimate the pairwise genetic
719   correlation (g_c) between each pair of DNEs, as well as between the nine DNEs and 9 BAGs of
720   multiple organ systems from our previous work[17] and 6 neurodegenerative and neuropsychiatric
721   disorders from PGC (**Supplementary Table 3a**). We used the precomputed LD scores from the
722   1000 Genomes of European ancestry. To ensure the suitability of the GWAS summary statistics,
723   we first checked that the selected study's population was European ancestry; we then guaranteed
724   a moderate SNP-based heritability h^2 estimate. Notably, LDSC corrects for sample overlap and
725   provides an unbiased estimate of genetic correlation[96]. Benjamini-Hochberg procedure was
726   performed to account for multiple comparisons.
727

728   **(f): Bayesian colocalization**: We used the R package (*coloc*) to investigate the genetic
729   colocalization signals between two traits at each genomic locus. We employed the Fully
730   Bayesian colocalization analysis using Bayes Factors (*coloc.abf*). This method examines the
731   posterior probability (PP.H4.ABF: Approximate Bayes Factor) to evaluate hypothesis *H4*, which
732   suggests the presence of a single shared causal variant associated with both traits within a
733   specific genomic locus. To determine the significance of the *H4* hypothesis, we set a threshold of
734   PP.H4.ABF>0.8[51]. All other parameters (e.g., the prior probability of p_{12}) were set as default. We
735   also performed relevant sensitivity analyses to check the robustness of our findings. For each
736   pair of traits, the genomic locus (*N*>100 SNPs) was defined by default from FUMA on the nine
737   DNEs, and then the *coloc* package extracted and harmonized the GWAS summary statistics
738   within this locus for the other trait.
739

740   **(g): Two-sample bidirectional Mendelian randomization**: We did not perform causal
741   inference between each pair of DNEs due to the overlapped populations and low sample sizes in
742   split-sample analyses.
743   We employed a bidirectional, two-sample Mendelian randomization using the
744   TwoSampleMR package[63] to infer the causal relationships between the nine DNEs and the eight
745   BAGs across nine human organ systems[17] (excluding the brain). The forward and inverse
746   Mendelian randomization was performed between each trait pair by switching the exposure and
747   outcome variables. We applied five different Mendelian randomization methods and reported the
748   results of inverse variance weighted (IVW) in the main text and the four others (i.e., Egger,
749   weighted median, simple mode, and weighted mode estimators) in the supplement.
750   We then performed Mendelian randomization between the nine DNEs and eleven chronic
751   diseases spanning the whole-body system. These diseases include four diseases from PGC (the
752   ASD and OCD GWAS summary statistics did not provide the allele frequency information) and
753   seven diseases unbiasedly curated in our previous work[17], which detailed a systematic procedure
754   to choose the appropriate traits. After harmonizing their GWAS summary statistics (using the
755   function *harmonise_data* from 2SampleMR), this resulted in 11 clinical traits with at least six

21

valid IVs (i.e., SNPs). The clinical traits included in our Mendelian randomization are presented in **Supplementary Table 11**. Benjamini-Hochberg correction was performed for all tested traits.

We performed several sensitivity analyses. First, a heterogeneity test was performed to check for violating the IV assumptions. Horizontal pleiotropy was estimated to navigate the violation of the IV's exclusivity assumption[97] using a funnel plot, single-SNP Mendelian randomization approaches, and Mendelian randomization Egger estimator[98]. Moreover, the leave-one-out analysis excluded one instrument (SNP) at a time and assessed the sensitivity of the results to individual SNP.

(h): PRS calculation for the nine DNEs: We calculated the PRS using the GWAS results from the split-sample analyses. The weights of the PRS were defined based on split1 data (base data), and the split2 GWAS summary statistics were used as the target data for PRS calculation. The QC steps for the base data are as follows: *i)* removal of duplicated and ambiguous SNPs for the base data; *ii)* clumping the base GWAS data; *iii)* pruning to remove highly correlated SNPs in the target data; *iv)* removal of high heterozygosity samples in the target data; *v)* removal of duplicated, mismatching and ambiguous SNPs in the target data. After rigorous QC, we used PLINK to generate PRS for the split2 population by adopting the classic C+T method (clumping + thresholding). To determine the "best-fit" PRS, we performed a linear regression using the PRS calculated at different P-value thresholds (0.001, 0.05, 0.1, 0.2, 0.3, 0.4, 0.5), controlling for age, sex, intracellular volume, and the first forty genetic PCs. For each DNE-PRS, we chose the P-value threshold with the highest incremental R^2 (**Supplementary Figure 19**). The comparison between PLINK and PRS-CS[99] is presented in **Supplementary Text 6** and **Figures 20–22**.

Disease, cognition, and mortality outcome prediction.

We employed logistic regression to calculate the incremental R-squared (R^2) statistics of the nine DNEs and PRSs to predict 14 disease categories (**a**), support vector machines to classify the healthy control participants from the disease groups (**b**), and Cox proportional hazard model to predict mortality outcomes (**c**). The patients for the 14 disease categories were defined based on the ICD-10 code from the UKBB website (Data field: 41270). The healthy control group included participants without any ICD-10-based disease diagnoses. The cognitive function data included 8 cognitive scores (Category: 100026), which were detailed in **Supplementary File 23**. The mortality outcome refers to the date of death: https://biobank.ndph.ox.ac.uk/ukb/field.cgi?id=40000.

(a): Pseudo R-squared (R^2) statistics of the logistic regression: We built a null model by including age, sex, and intracranial volume as predictors and the disease as the outcome variable. The alternative model took the disease-specific DNE or PRS as one additional predictor. The incremental R^2 was calculated as the difference between the pseudo R^2 of the alternative model and that of the null model, implemented by the *PseudoR2* function from the *DescTools* R package (v 0.99.38). For the nine PRSs, we used the PRS target sample (*N*=15,891). For the nine DNEs, we calculated the incremental R^2 using the entire UKBB sample (*N*=39,178) and the PRS target sample (*N*=15,891). We reported the incremental R^2 of the DNE/PRS in the main manuscript (**Fig. 5a** and **b**). Other metrics, including R^2 of the null and the alternative model, sample sizes, and the β values of other covariates, are presented in **Supplementary File 20-21**.

22

(b): Support vector machines to classify patients vs. controls: Using the PRS target sample (N=15,891), we used 10000 participants in a nested cross-validation (CV) procedure (i.e., CV training/validation/test datasets) to select the hyperparameter C in SVM. In addition, we held out 5581 participants as an independent test dataset. In **Fig. 5c**, we only presented the classification accuracy from the independent test dataset. The nested cross-validation (CV) procedure[100] involved an outer loop repeated 50 times, where 80% of the data were randomly selected for training/validation and 20% for testing. Within each outer loop iteration, an inner loop used 80% of the training/validation data for a 10-fold training/validation split. Critically, the model trained on the training/validation/test datasets generalized to the independent test dataset (**Fig. 5c**). **Supplementary File 22** contains various metrics, including balanced accuracy, sensitivity, specificity, negative predictive value (NPV), positive predictive value (PPV), and sample sizes for the independent dataset (*Ind. accuracy*) and the CV training/validation/test datasets (*CV accuracy*). We did not statistically compare the performance between different machine learning models as this is a complex matter without a universal solution. A standard *t*-test on cross-validation results is too liberal and should not be applied, as shown by Nadeau and Bengio[101]. The corrected resampled *t*-test[101] was proposed, but it depends on the data and the cross-validation setup.

(c): Support vector regression to predict cognitive scores: Using the PRS target sample (N=15,891), we used 10000 participants in a nested cross-validation (CV) procedure (i.e., CV training/validation/test datasets) to select the hyperparameter C in SVM. In addition, we held out 5581 participants (some had missing values depending on specific cognitive scores) as an independent test dataset (*Ind. r*). In **Fig. 5d**, we only presented Pearson's *r* from the independent test dataset. The same nested CV procedure was used, as mentioned above. Likewise, **Supplementary File 23** encompasses a range of metrics, including mean absolute error, P-values, and sample sizes, pertaining to the independent dataset (*Ind. r)* and the CV training/validation/test datasets (*CV r*).

(d): Cox proportional hazard model to predict the date of death: To evaluate the predictive capacity of individual DNE and PRS for mortality risk, we employed a Cox proportional hazard model while adjusting for covariates such as age and sex. The hazard ratio (HR) was calculated and reported as the effect size measure that indicates the influence of each DNE or PRS on mortality risk. Furthermore, we incrementally added the most predictive DNE or PRS to the Cox model to determine when the model's performance reached saturation. The concordance index (CI) was utilized to assess the model's performance using a 5-fold cross-validation procedure. All survival analyses were conducted using the *lifelines* (v0.25.7) Python package.

23

Data Availability

837

838 The GWAS summary statistics and pre-trained AI models from this study are publicly accessible
839 via the MEDICINE Knowledge Portal (https://labs-laboratory.com/medicine/) and Synapse
840 (https://www.synapse.org/Synapse:syn64923248/wiki/630992[102]). Genomic loci annotation used
841 data from FUMA (https://fuma.ctglab.nl/). UKBB data can be requested at
842 https://www.ukbiobank.ac.uk/. GWAS summary data from the Psychiatric Genomics
843 Consortium (PGC) can be accessed at https://pgc.unc.edu/. MUSE atlas is generated via the
844 pipeline at: https://github.com/CBICA/MUSE.

Code Availability

The software and resources used in this study are all publicly available:

- *MLNI*[103] *(HYDRA)*: https://github.com/anbai106/mlni, DNEs for ASD1-3, LLD1-2, SCZ1-2
- *Surreal-GAN*[104]: https://github.com/zhijian-yang/SurrealGAN, DNEs for AD1-2

25

Acknowledgments

26

864 **Competing Interests Statement**

865 None
866

867 **Author Contributions Statement**

868 Dr. Wen has full access to all the data in the study and takes responsibility for the integrity of the
869 data and the accuracy of the data analysis.
870 *Study concept and design*: Wen, Davatzikos
871 *Acquisition, analysis, or interpretation of data*: all authors
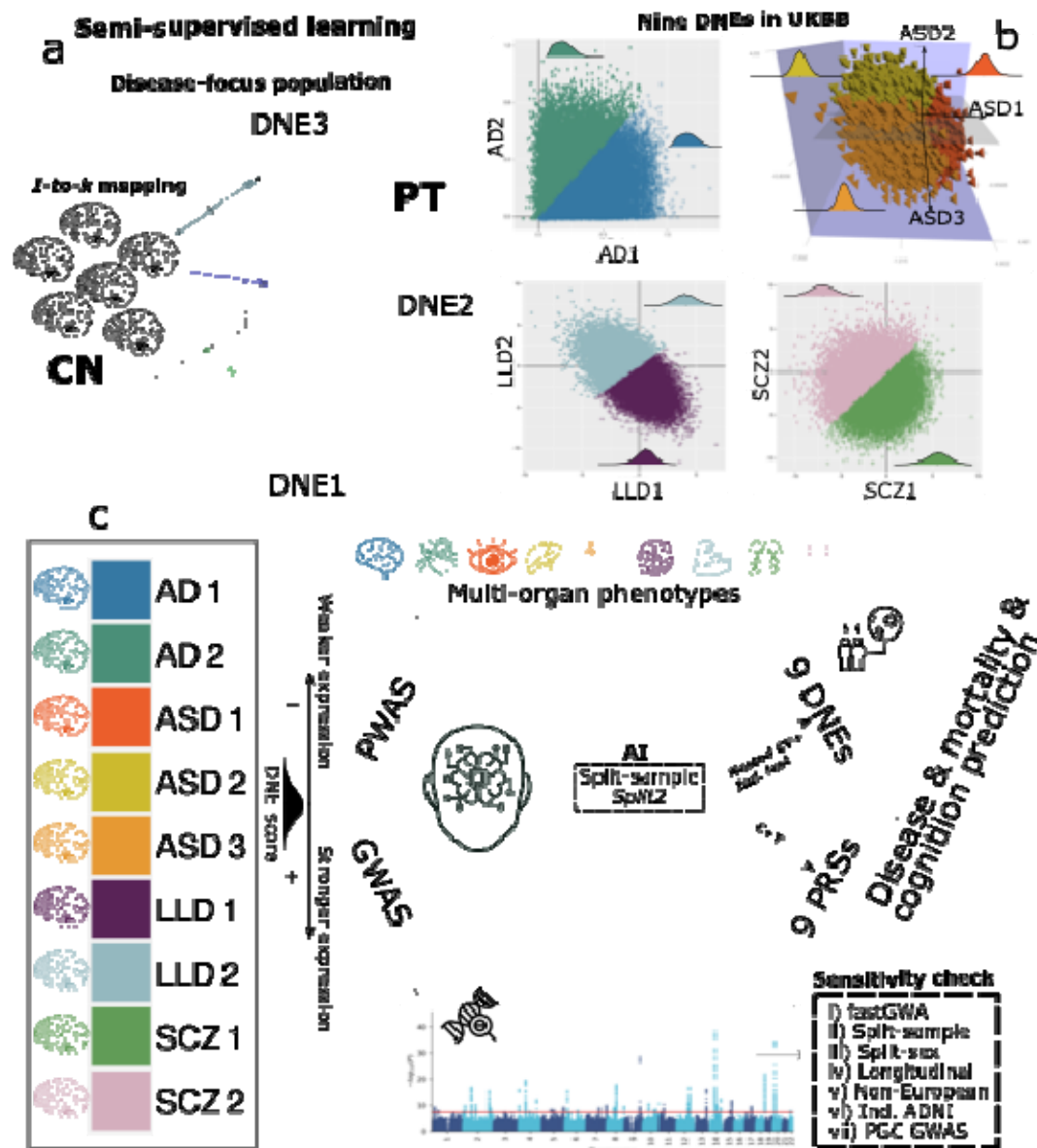872 *Drafting of the manuscript*: Wen
873 *Critical revision of the manuscript for important intellectual content*: all authors
874 *Statistical analysis*: Wen
875

876 **Figure Legends/Captions**

877 **Figure 1**: **Study workflow**

878

30

879   **a**) The concept of semi-supervised learning methods used in this study. These AI methods model
880   the patterns and transformations from the healthy control (CN) to the patient (PT) domain, thus
881   capturing variations related to underlying disease pathology. Nine DNEs previously
882   published[12,2,1,13] from four disease-focused, case-control studies were investigated. **b**) The
883   expression of the nine DNEs in the UK Biobank (UKBB) general population. The trained models
884   were then applied to the UKBB population to quantify the expression of the neuroanatomical
885   patterns of the nine DNEs at individual levels; a higher DNE score indicates a greater expression
886   (manifestation/presence) of the respective neuroanatomical pattern. For example, the blue
887   samples express predominantly AD2, whereas the pink samples express predominantly SCZ2.
888   The kernel density estimate for each DNE is shown. Of note, AD1-2 DNEs are from the Surreal-
889   GAN[14] model and others from the HYDRA[87] model, resulting in varying DNE score ranges by
890   modeling. Overall, lower scores imply milder imaging pattern expressions. **c**) Phenome- and
891   genome-wide analyses were performed on the nine DENs. Phenome-wide association studies
892   (PWAS) were conducted to associate the nine DNEs with phenotypes across nine organ systems,
893   cognition, and lifestyle factors. Genome-wide association studies (GWAS) were performed to
894   investigate associations between the nine DNEs and common genetic variants (SNPs). Finally,
895   the nine DNEs and their polygenic risk scores predicted 14 disease categories (ICD-10-based), 8
896   cognitive scores, and mortality. CN: healthy control; PT: patient.
897

898 **Figure 2**: **Phenome-wide associations of the nine DNEs**

32

899

33
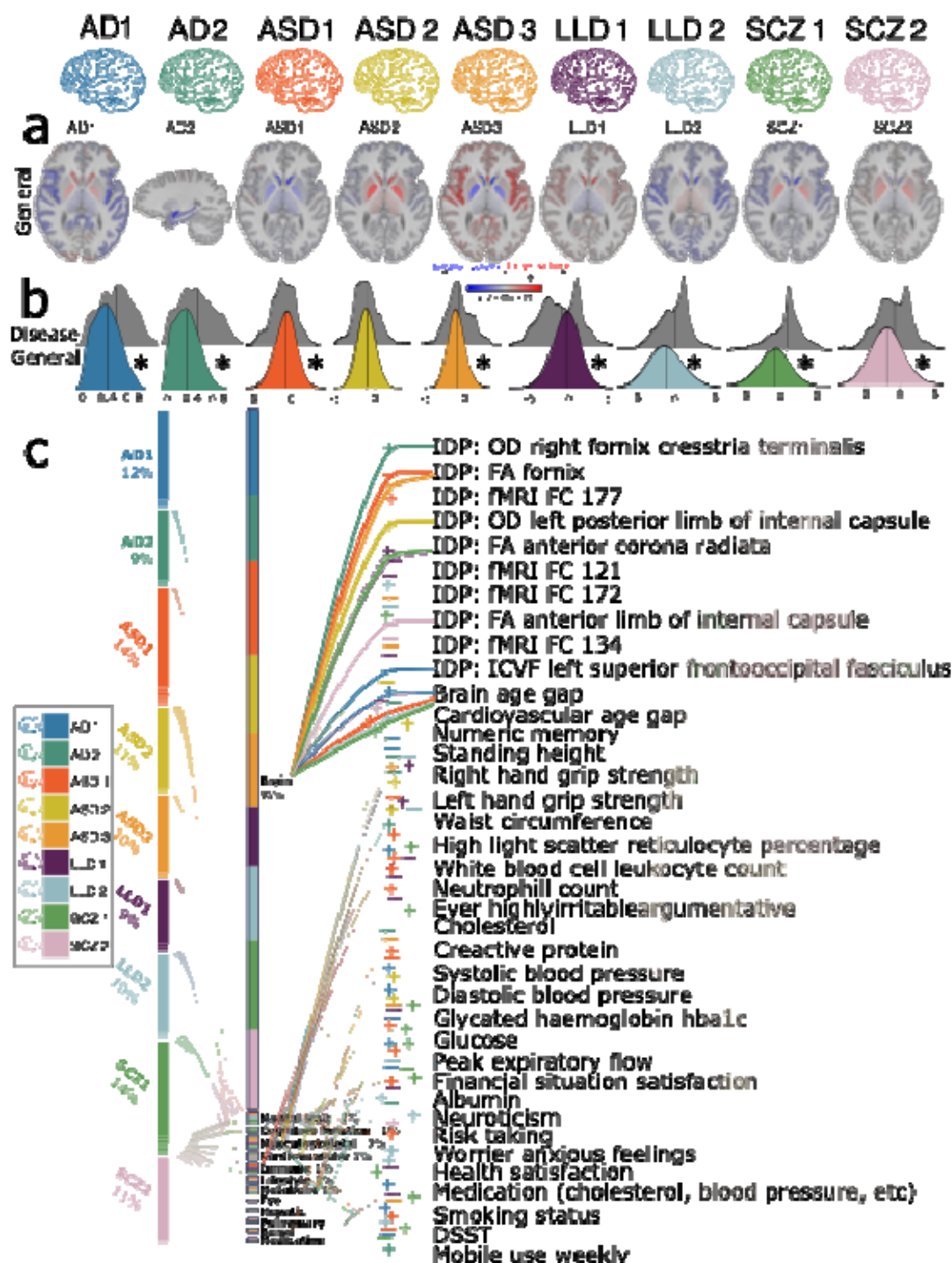
900   **a**) The neuroanatomical patterns of the nine DNEs were manifested in the UKBB general
901   population and were concordant with the patterns initially derived from the original disease
902   populations[12,2,1,13]. A linear regression model was applied to the 119 gray matter regions of
903   interest (ROIs) derived from T1-weighted MRI data while accounting for various covariates. We
904   present the β coefficients of the ROIs that withstood the Bonferroni correction. Positive
905   correlations are depicted using warm reddish colors, while cold blue colors represent negative
906   correlations. For AD2, we showed the sagittal view to visualize the hippocampus and medial
907   temporal lobe. Sample sizes range from 40,534 to 40,981 to derive these results. **b)** The nine
908   DNEs are over-expressed (i.e., a higher mean of the DNE score in the population) and under-
909   expressed (i.e., a lower mean of the DNE score) in the general population compared to the
910   disease populations. The kernel density estimates of the nine DNEs are shown for both the
911   training dataset (gray-colored in patients) and the independent test dataset from the UK Biobank
912   (UKBB). Significant differences that survived the Bonferroni corrections between the training
913   and independent test datasets (two-sampled t-test) are denoted with the symbol *. Sample sizes
914   range from 38,534 to 38,981 to derive these results in UKBB and from 307 to 1510 in the
915   original diseased populations. **c**) Phenome-wide associations (PWAS) between the nine DNEs
916   (left panel) and 611 phenotypes (middle panel) are dominated by brain phenotypic measures. The
917   right panel shows representative phenotypes linked to multiple phenotype categories with the
918   highest statistical significance after the Bonferroni correction (two-sided t-test P-
919   value<0.05/611). A thicker colored line corresponds to a higher value of -log10(P-value). The
920   symbols "+" and "-" represent positive and negative correlations. IDP: imaging-derived
921   phenotype; OD: orientation dispersion; FA: fractional anisotropy; ICVF: intracellular volume
922   fraction; FC: functional connectivity; DSST: digit symbol substitution test. Sample sizes range
923   from 722 to 39,174 after merging the DNEs and these phenotypes. The illustration of the human
924   anatomy is from NIH BIOART Source (https://bioart.niaid.nih.gov/).
925

926 **Figure 3**: **Genome-wide associations of the nine DNEs**

35

927

36
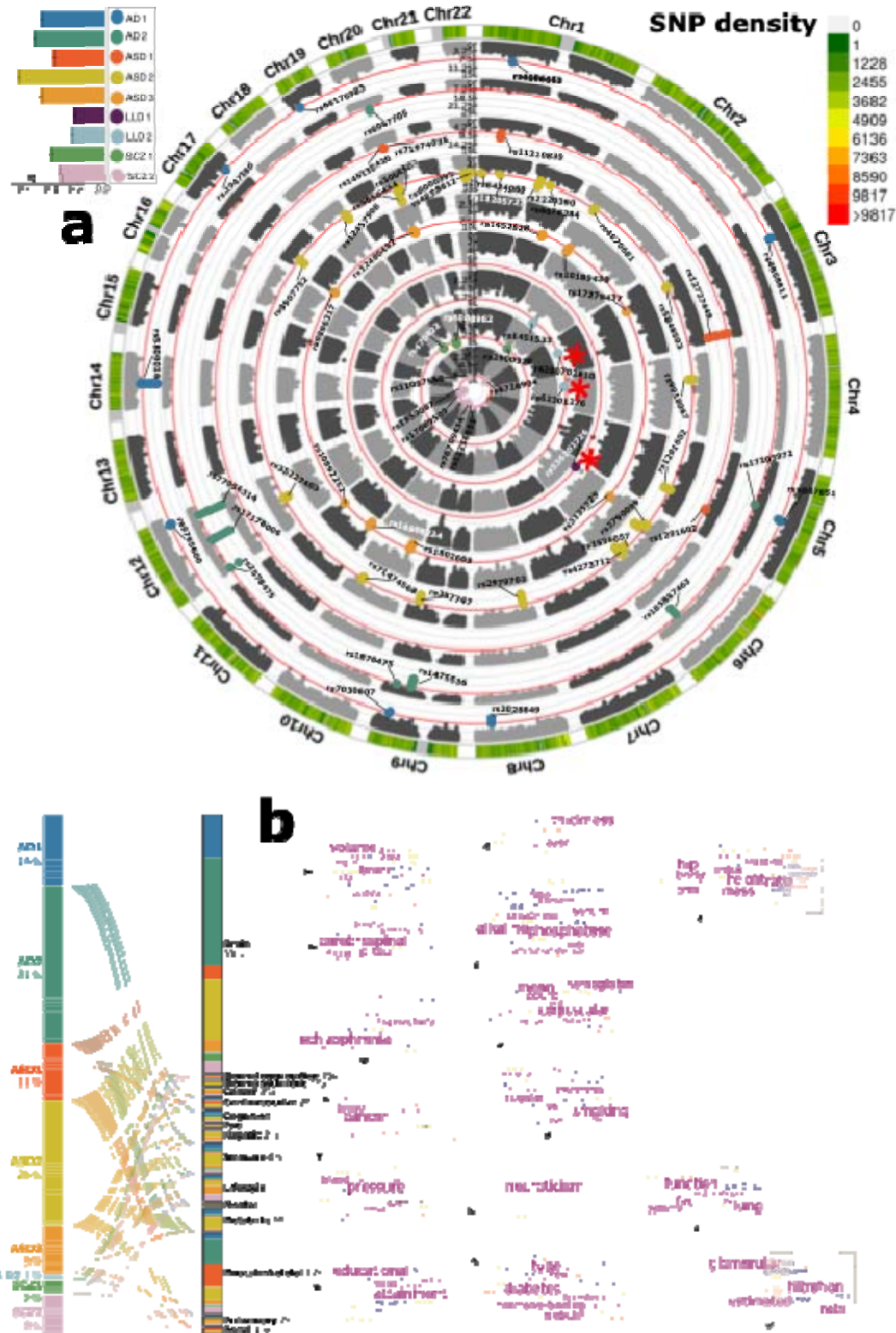
928 **a**) Genome-wide associations identified 66 (10, 8, 5, 21, 9, 1, 3, 3, 6 for the nine DNEs) genomic
929 loci (P-value<5x10^{-8}) associated with the nine DNEs. Using the top lead SNP, we denoted each
930 genomic loci linked to the 9 DNEs. Red * symbols indicate that the locus LD has not been
931 previously associated with any trait in the EMBL-EBI GWAS catalog. The left legend indicates
932 the significant SNP-based heritability (h^2) for the nine DNEs; the right legend represents the SNP
933 density of our genetic data throughout the human genome. GWAS was performed using the
934 Genome Reference Consortium Human Build 37 (GRCh37). These GWASs included 31,976
935 participants of European ancestry. **b**) Phenome-wide association query of the previously
936 identified genomic loci (left panel) in the EMBL-EBI GWAS Catalog (via FUMA 1.4.2) shows a
937 brain-dominant genetic architecture. We categorized all clinical traits (middle panel) into several
938 high-level categories linked to multiple organ systems, neurodegenerative and neuropsychiatric
939 disorders, lifestyle factors, etc. We then show the keyword cloud plots for each category (right
940 panel). The illustration of the human anatomy is from NIH BIOART Source
941 (https://bioart.niaid.nih.gov/).
942

943   **Figure 4**: **The genetic correlation, colocalization, and causal networks of the nine DNEs**
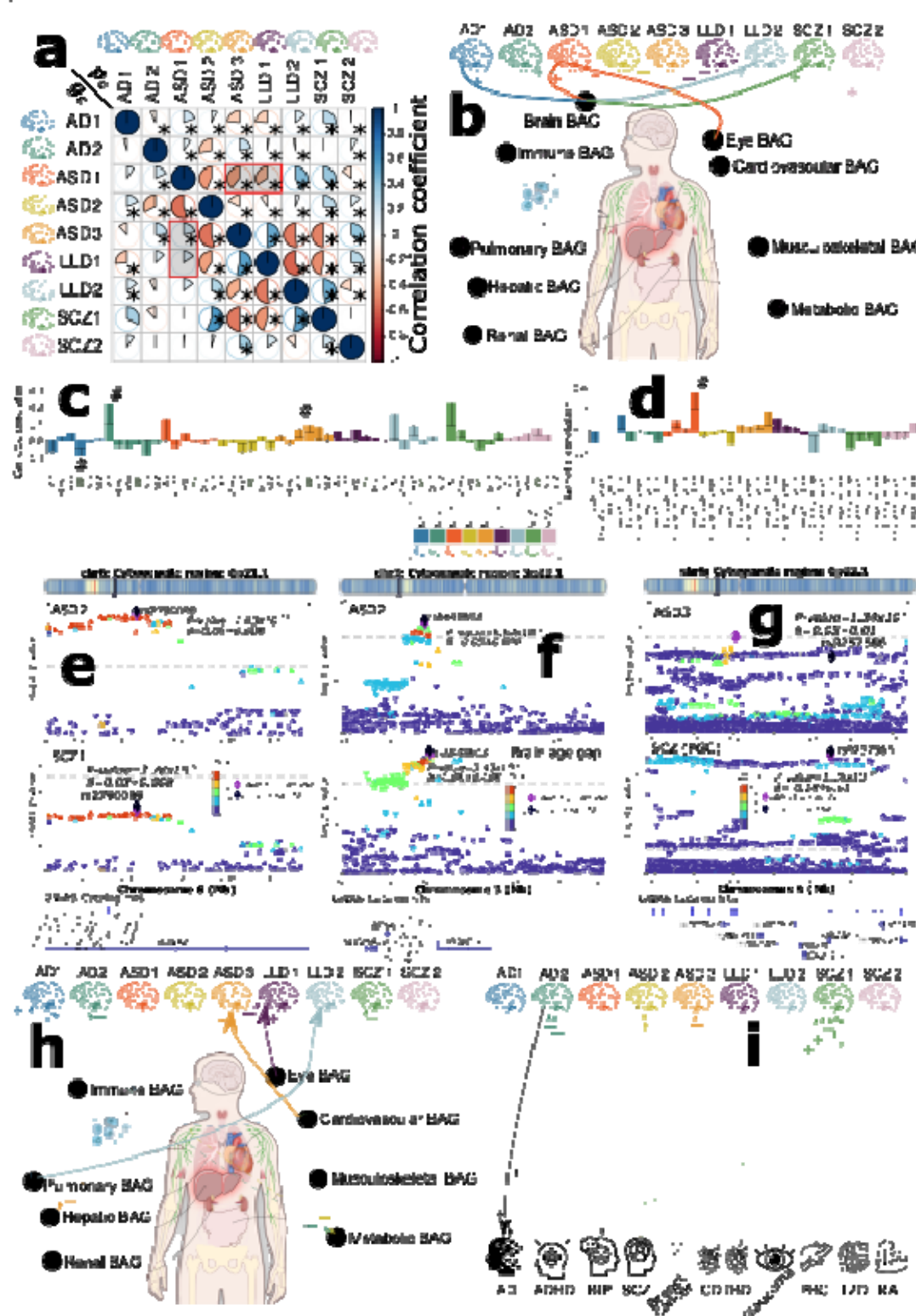
a) The genetic correlation between two DNEs (g_c, lower triangle) mirrors their phenotypic correlation (p_c, upper triangle). Red-shadowed rectangles highlight two exceptions. The symbol * indicates significant results after the Benjamini-Hochberg correction. The symbol # indicates nominal significance. **b**) genetic correlations between the nine DNEs and nine biological age gaps (BAG) for nine human organ systems[17]. **c**) genetic correlations between the nine DNEs and six neurodegenerative and neuropsychiatric disorders. The bar plots display the estimated mean genetic correlation along with its standard error. **d**) genetic correlations between the nine DNEs and four traits related to lifestyle factors and cognition. The bar plots display the estimated mean genetic correlation along with its standard error. A two-sided p-value is used to determine statistical significance. **e**) genetic colocalization was evidenced at one locus (6p21.1) between ASD2 and SCZ1. The signed PP.H4.ABF (0.92) denotes the posterior probability (PP) of hypothesis H4, which suggests that both traits share the same causal SNP (rs2790099). A positive PP indicates concordant β values for both DNEs, while a negative PP implies opposite β values. **f**) genetic colocalization was evidenced at one locus (3p.22.1) between ASD2 and brain BAG: PP.H4.ABF=0.95 with the cause SNP rs5848503. **g**) genetic colocalization was evidenced at one locus (6p.22.1) between ASD3 and SCZ case-control GWAS[45] from PGC (European ancestry): PP.H4.ABF=0.82 with the cause SNP rs9257566. **h**) the causal network of the nine DNEs with the eight multi-organ BAGs. Solid arrow lines (from the exposure to the outcome variables) indicate significant causal relationships after the Benjamini-Hochberg correction; dotted arrow lines show nominal significance (P-value<0.05). The symbols + (OR>1 and g_c>0) and – (OR<1 and g_c<0) represent a positive relationship between the two traits. **i**) the causal network of the nine DNEs with the eleven chronic diseases (e.g., AD, ADHD, BIP, and SCZ from PGC). Abbreviation: AD: Alzheimer's disease; ADHD: Attention-deficit/hyperactivity disorder; ASD: autism spectrum disorder; BIP: bipolar disorder; SCZ: schizophrenia; OCD: Obsessive-compulsive disorder; RA: rheumatoid arthritis; CD: Crohn's disease; T2D: type 2 diabetes; IBD: inflammatory bowel disease; PBC: Primary biliary cirrhosis. The illustration of the human anatomy is from NIH BIOART Source (https://bioart.niaid.nih.gov/).

40

973 **Figure 5**: **Additional prediction power of the nine DNEs and PRSs for 14 systemic diseases,**
974 **cognition, and mortality outcomes**
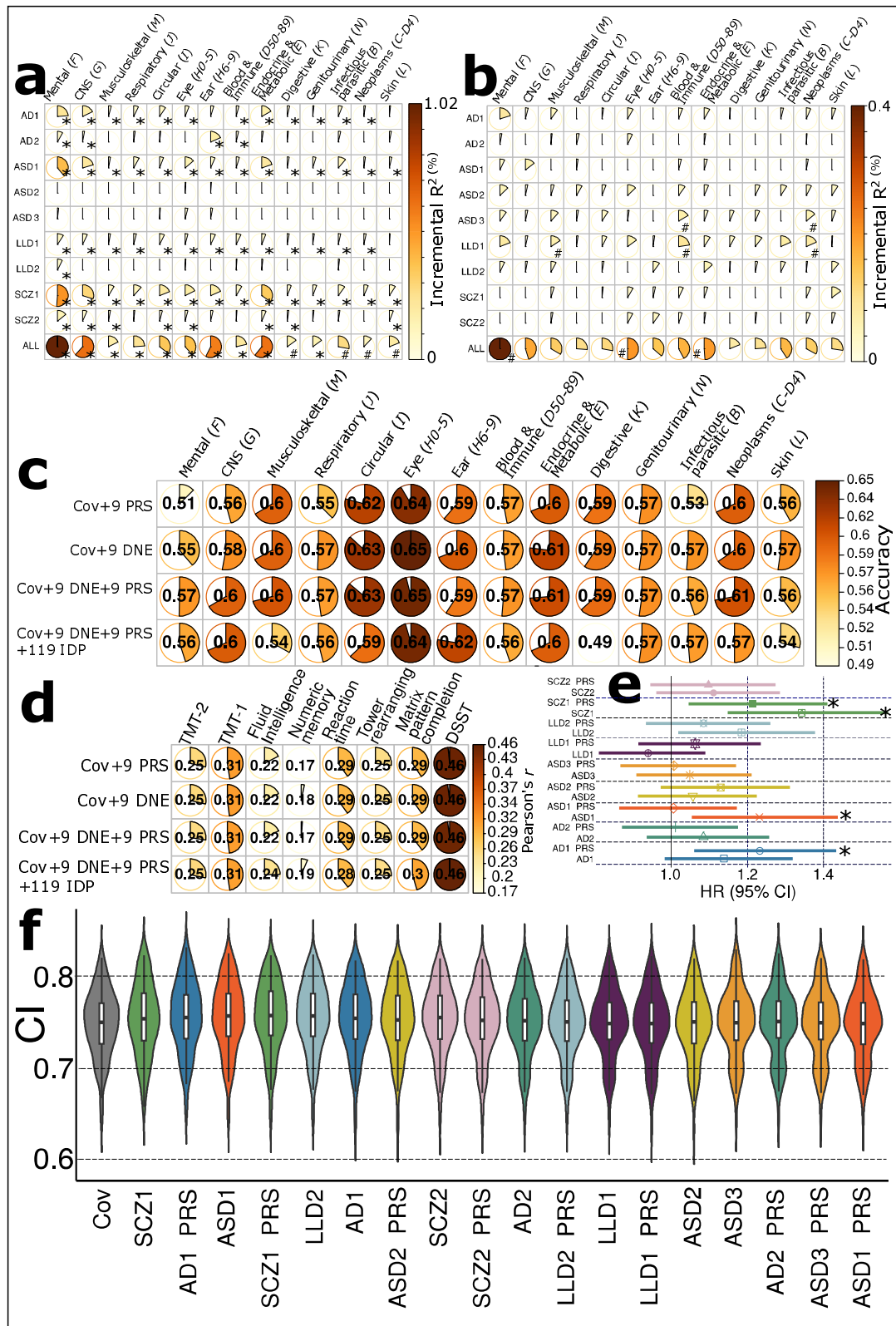
976   **a**) The incremental R-squared (R^2) values of the nine DNEs for predicting 14 systemic disease

977   categories were assessed using the entire UKBB sample, with N=39,178 participants as

978   independent test data. The results focusing only on the PRS target population (N=15,891) can be

979   found in **Supplementary Figure 18**. "ALL" indicates the incremental R^2 contributed by

980   combining the nine DNEs. **b**) The incremental R^2 of the PRS of the nine DNEs to predict 14

981   systemic diseases based on the ICD-10 code using only the PRS target sample. **c**) In the PRS

982   target sample, disease classification accuracy from the independently hold-out test data (N=5581)

983   was assessed using nested cross-validated support vector machines in the training/validation/test

984   data (N=10,000) by fitting various sets of features (Cov indicates age and sex). **d**) In the PRS

985   target sample, cognitive score prediction accuracy (Peasrson's r) from the independently hold-out

986   test data (3632<N<5570) was assessed using nested cross-validated support vector regression

987   models. **e**) The SCZ1, SCZ1-PRS, AD1-PRS, and ASD1 show significant associations with the

988   risk of mortality in the PRS target sample. Age and sex were included as covariates in the Cox

989   proportional hazard model. **f**) The nine DNEs and PRSs were cumulatively included as features

990   in cross-validation for mortality risk prediction. The symbol * indicates significant results that

991   survived the Benjamini-Hochberg correctionThe symbol **#** indicates nominal significance. All P

992   values are two-sided. HR: hazard ratio; CI: concordance index; DSST: digit symbol substitution

993   test; TMT: trail-making test. The box plots display the mean of the CIs, while the violin plots

994   illustrate their distribution during cross-validation.

995

References

996

1. Hwang, G. *et al.* Assessment of Neuroanatomical Endophenotypes of Autism Spectrum Disorder and Association With Characteristics of Individuals With Schizophrenia and the General Population. *JAMA Psychiatry* (2023) doi:10.1001/jamapsychiatry.2023.0409.

2. Wen, J. *et al.* Characterizing Heterogeneity in Neuroimaging, Cognition, Clinical Symptoms, and Genetics Among Patients With Late-Life Depression. *JAMA Psychiatry* (2022) doi:10.1001/jamapsychiatry.2022.0020.

3. Young, A. L. *et al.* Uncovering the heterogeneity and temporal complexity of neurodegenerative diseases with Subtype and Stage Inference. *Nat Commun* **9**, 4273 (2018).

4. Yang, Z. *et al.* A deep learning framework identifies dimensional representations of Alzheimer's Disease from brain structure. *Nat Commun* **12**, 7065 (2021).

5. Zhang, X. *et al.* Bayesian model reveals latent atrophy factors with dissociable cognitive trajectories in Alzheimer's disease. *Proc Natl Acad Sci USA* **113**, E6535–E6544 (2016).

6. Vogel, J. W. *et al.* Four distinct trajectories of tau deposition identified in Alzheimer's disease. *Nat Med* **27**, 871–881 (2021).

7. Wen, J. *et al.* Multi-scale semi-supervised clustering of brain images: Deriving disease subtypes. *Med Image Anal* **75**, 102304 (2021).

8. Ferreira, D., Nordberg, A. & Westman, E. Biological subtypes of Alzheimer disease: A systematic review and meta-analysis. *Neurology* **94**, 436–448 (2020).

9. Hodson, R. Precision medicine. *Nature* **537**, S49–S49 (2016).

10. Davatzikos, C. *et al.* Precision diagnostics based on machine learning-derived imaging signatures. *Magnetic Resonance Imaging* **64**, 49–61 (2019).

44

11. Leonenko, G. *et al.* Identifying individuals with high risk of Alzheimer's disease using polygenic risk scores. *Nat Commun* **12**, 4506 (2021).

12. Wen, J. *et al.* Genetic and clinical correlates of two neuroanatomical AI dimensions in the Alzheimer's disease continuum. *Transl Psychiatry* **14**, 1–14 (2024).

13. Chand, G. B. *et al.* Two distinct neuroanatomical subtypes of schizophrenia revealed using machine learning. *Brain* **143**, 1027–1038 (2020).

14. Yang, Z., Wen, J. & Davatzikos, C. Surreal-GAN:Semi-Supervised Representation Learning via GAN for uncovering heterogeneous disease-related imaging patterns. *ICLR* (2021).

15. Wingo, T. S. *et al.* Shared mechanisms across the major psychiatric and neurodegenerative diseases. *Nat Commun* **13**, 4314 (2022).

16. Anttila, V. Analysis of shared heritability in common disorders of the brain. *Science* **360**, eaap8757 (2018).

17. Wen, J. *et al.* The genetic architecture of biological age in nine human organ systems. *Nat Aging* 1–18 (2024) doi:10.1038/s43587-024-00662-8.

18. Wen, J. Multiorgan biological age shows that no organ system is an island. *Nat Aging* 1–2 (2024) doi:10.1038/s43587-024-00690-4.

19. Wen, J. *et al.* The genetic architecture of multimodal human brain age. *Nat Commun* **15**, 2604 (2024).

20. Boquet-Pujadas, A. *et al.* MUTATE: a human genetic atlas of multiorgan artificial intelligence endophenotypes using genome-wide association summary statistics. *Briefings in Bioinformatics* **26**, bbaf125 (2025).

45

1040   21. Petersen, R. C. *et al.* Alzheimer's Disease Neuroimaging Initiative (ADNI): Clinical

1041   characterization. *Neurology* **74**, 201–209 (2010).

1042   22. Di Martino, A. *et al.* Enhancing studies of the connectome in autism using the autism brain

1043   imaging data exchange II. *Sci Data* **4**, 170010 (2017).

1044   23. Chand, G. B. *et al.* Two distinct neuroanatomical subtypes of schizophrenia revealed using

1045   machine learning. *Brain* **143**, 1027–1038 (2020).

1046   24. Wen, J. *et al.* Subtyping Brain Diseases from Imaging Data. in *Machine Learning for Brain*

1047   *Disorders* (ed. Colliot, O.) 491–510 (Springer US, New York, NY, 2023). doi:10.1007/978-

1048   1-0716-3195-9_16.

1049   25. Kendler, K. & Neale, M. Endophenotype: a conceptual analysis. *Mol Psychiatry* **15**, 789–

1050   797 (2010).

1051   26. Cannon, T. D. & Keller, M. C. Endophenotypes in the Genetic Analyses of Mental

1052   Disorders. *Annual Review of Clinical Psychology* **2**, 267–290 (2006).

1053   27. Gottesman, I. I. & Gould, T. D. The endophenotype concept in psychiatry: etymology and

1054   strategic intentions. *Am J Psychiatry* **160**, 636–645 (2003).

1055   28. Bycroft, C. *et al.* The UK Biobank resource with deep phenotyping and genomic data.

1056   *Nature* **562**, 203–209 (2018).

1057   29. Alfaro-Almagro, F. *et al.* Image processing and Quality Control for the first 10,000 brain

1058   imaging datasets from UK Biobank. *Neuroimage* **166**, (2018).

1059   30. Elliott, L. T. *et al.* Genome-wide association studies of brain imaging phenotypes in UK

1060   Biobank. *Nature* **562**, 210–216 (2018).

1061   31. Wen, J. *et al.* Genomic loci influence patterns of structural covariance in the human brain.

1062   *Proceedings of the National Academy of Sciences* **120**, e2300842120 (2023).

46

1063   32.   Guan, H. & Liu, M. Domain Adaptation for Medical Image Analysis: A Survey. *IEEE*

1064   *Trans Biomed Eng* **69**, 1173–1185 (2022).

1065   33.   Zhang, H., Schneider, T., Wheeler-Kingshott, C. A. & Alexander, D. C. NODDI: Practical

1066   in vivo neurite orientation dispersion and density imaging of the human brain. *NeuroImage*

1067   **61**, 1000–1016 (2012).

1068   34.   Joseph, C., Wang, L., Wu, R., Manning, K. J. & Steffens, D. C. Structural brain changes

1069   and neuroticism in late-life depression: a neural basis for depression subtypes. *Int*

1070   *Psychogeriatr* **33**, 515–520 (2021).

1071   35.   Tian, Y. E. *et al.* Heterogeneous aging across multiple organ systems and prediction of

1072   chronic disease and mortality. *Nat Med* 1–11 (2023) doi:10.1038/s41591-023-02296-6.

1073   36.   McCracken, C. *et al.* Multi-organ imaging demonstrates the heart-brain-liver axis in UK

1074   Biobank participants. *Nat Commun* **13**, 7839 (2022).

1075   37.   Bulik-Sullivan, B. K. *et al.* LD Score regression distinguishes confounding from

1076   polygenicity in genome-wide association studies. *Nat Genet* **47**, 291–295 (2015).

1077   38.   Yang, J., Lee, S. H., Goddard, M. E. & Visscher, P. M. GCTA: A Tool for Genome-wide

1078   Complex Trait Analysis. *Am J Hum Genet* **88**, 76–82 (2011).

1079   39.   Jiang, L., Zheng, Z., Fang, H. & Yang, J. A generalized linear mixed model association tool

1080   for biobank-scale data. *Nat Genet* **53**, 1616–1621 (2021).

1081   40.   Jiang, L. *et al.* A resource-efficient tool for mixed model association analysis of large-scale

1082   data. *Nat Genet* **51**, 1749–1755 (2019).

1083   41.   Wightman, D. P. *et al.* A genome-wide association study with 1,126,563 individuals

1084   identifies new risk loci for Alzheimer's disease. *Nat Genet* **53**, 1276–1282 (2021).

42. Demontis, D. *et al.* Genome-wide analyses of ADHD identify 27 risk loci, refine the genetic architecture and implicate several cognitive domains. *Nat Genet* **55**, 198–208 (2023).

43. Grove, J. *et al.* Identification of common genetic risk variants for autism spectrum disorder. *Nat Genet* **51**, 431–444 (2019).

44. Mullins, N. *et al.* Genome-wide association study of more than 40,000 bipolar disorder cases provides new insights into the underlying biology. *Nat Genet* **53**, 817–829 (2021).

45. Trubetskoy, V. *et al.* Mapping genomic loci implicates genes and synaptic biology in schizophrenia. *Nature* **604**, 502–508 (2022).

46. International Obsessive Compulsive Disorder Foundation Genetics Collaborative (IOCDF-GC) and OCD Collaborative Genetics Association Studies (OCGAS). Revealing the complex genetic architecture of obsessive-compulsive disorder using meta-analysis. *Mol Psychiatry* **23**, 1181–1188 (2018).

47. O'Donovan, M. C. What have we learned from the Psychiatric Genomics Consortium. *World Psychiatry* **14**, 291–293 (2015).

48. Cheverud, J. M. A comparison of genetic and pehnotypic correlations. *Evolution* **42**, 958–968 (1988).

49. Leeuw, C. A. de, Mooij, J. M., Heskes, T. & Posthuma, D. MAGMA: Generalized Gene-Set Analysis of GWAS Data. *PLOS Computational Biology* **11**, e1004219 (2015).

50. McCutcheon, R. A., Krystal, J. H. & Howes, O. D. Dopamine and glutamate in schizophrenia: biology, symptoms and treatment. *World Psychiatry* **19**, 15–33 (2020).

51. Giambartolomei, C. *et al.* Bayesian Test for Colocalisation between Pairs of Genetic Association Studies Using Summary Statistics. *PLOS Genetics* **10**, e1004383 (2014).

1108   52. Hordyjewska-Kowalczyk, E. *et al.* Functional analysis of novel RUNX2 mutations

1109   identified in patients with cleidocranial dysplasia. *Clin Genet* **96**, 429–438 (2019).

1110   53. Wamsley, B. *et al.* Molecular cascades and cell type–specific signatures in ASD revealed

1111   by single-cell genomics. *Science* **384**, eadh2602 (2024).

1112   54. Ayalew, M. *et al.* Convergent functional genomics of schizophrenia: from comprehensive

1113   understanding to genetic risk prediction. *Mol Psychiatry* **17**, 887–905 (2012).

1114   55. Siokas, V. *et al.* Myelin-associated oligodendrocyte basic protein rs616147 polymorphism

1115   as a risk factor for Parkinson's disease. *Acta Neurologica Scandinavica* **145**, 223–228

1116   (2022).

1117   56. Arnold, S. E. *et al.* Dysregulation of olfactory receptor neuron lineage in schizophrenia.

1118   *Arch Gen Psychiatry* **58**, 829–835 (2001).

1119   57. Turetsky, B. I., Moberg, P. J., Arnold, S. E., Doty, R. L. & Gur, R. E. Low olfactory bulb

1120   volume in first-degree relatives of patients with schizophrenia. *Am J Psychiatry* **160**, 703–

1121   708 (2003).

1122   58. Almandil, N. B. *et al.* Exome-wide analysis identify multiple variations in olfactory

1123   receptor genes (OR12D2 and OR5V1) associated with autism spectrum disorder in Saudi

1124   females. *Frontiers in Medicine* **10**, (2023).

1125   59. Kuo, P.-H. *et al.* Genome-Wide Association Study for Autism Spectrum Disorder in

1126   Taiwanese Han Population. *PLOS ONE* **10**, e0138695 (2015).

1127   60. Warnica, W. *et al.* Copy number variable microRNAs in schizophrenia and their

1128   neurodevelopmental gene targets. *Biol Psychiatry* **77**, 158–166 (2015).

1129   61. Christen-Zaech, S. *et al.* Early Olfactory Involvement in Alzheimer's Disease. *Canadian*

1130   *Journal of Neurological Sciences* **30**, 20–25 (2003).

49

1131   62. Murphy, C. Olfactory and other sensory impairments in Alzheimer disease. *Nat Rev Neurol*

1132   **15**, 11–24 (2019).

1133   63. Hemani, G. *et al.* The MR-Base platform supports systematic causal inference across the

1134   human phenome. *eLife* **7**, e34408 (2018).

1135   64. Sanderson, E. *et al.* Mendelian randomization. *Nat Rev Methods Primers* **2**, 1–21 (2022).

1136   65. 23andMe Research Team *et al.* Genome-wide association study of depression phenotypes

1137   in UK Biobank identifies variants in excitatory synaptic pathways. *Nat Commun* **9**, 1470

1138   (2018).

1139   66. Navari, S. & Dazzan, P. Do antipsychotic drugs affect brain structure? A systematic and

1140   critical review of MRI findings. *Psychol Med* **39**, 1763–1777 (2009).

1141   67. Chopra, S. *et al.* Differentiating the effect of antipsychotic medication and illness on brain

1142   volume reductions in first-episode psychosis: A Longitudinal, Randomised, Triple-blind,

1143   Placebo-controlled MRI Study. *Neuropsychopharmacol.* **46**, 1494–1501 (2021).

1144   68. Zeldovich, L. Cold parenting? Childhood schizophrenia? How the diagnosis of autism has

1145   evolved over time. *Science* doi: 10.1126/science.aau1206 (2018).

1146   69. Moreau, C. A. *et al.* Dissecting autism and schizophrenia through neuroimaging genomics.

1147   *Brain* **144**, 1943–1957 (2021).

1148   70. Fu, Z. *et al.* Dynamic functional network reconfiguration underlying the pathophysiology of

1149   schizophrenia and autism spectrum disorder. *Human Brain Mapping* **42**, 80–94 (2021).

1150   71. Bereczki, E. *et al.* Synaptic markers of cognitive decline in neurodegenerative diseases: a

1151   proteomic approach. *Brain* **141**, 582–595 (2018).

1152   72. Jiang, C.-C. *et al.* Signalling pathways in autism spectrum disorder: mechanisms and

1153   therapeutic implications. *Sig Transduct Target Ther* **7**, 1–36 (2022).

50

1154   73. Chi, S., Yu, J.-T., Tan, M.-S. & Tan, L. Depression in Alzheimer's disease: epidemiology,

1155   mechanisms, and management. *J Alzheimers Dis* **42**, 739–755 (2014).

1156   74. Dafsari, F. S. & Jessen, F. Depression—an underrecognized target for prevention of

1157   dementia in Alzheimer's disease. *Transl Psychiatry* **10**, 1–13 (2020).

1158   75. Ly, M. *et al.* Late-life depression and increased risk of dementia: a longitudinal cohort

1159   study. *Transl Psychiatry* **11**, 1–10 (2021).

1160   76. Lalousis, P. A. *et al.* Neurobiologically Based Stratification of Recent-Onset Depression

1161   and Psychosis: Identification of Two Distinct Transdiagnostic Phenotypes. *Biological*

1162   *Psychiatry* **92**, 552–562 (2022).

1163   77. Woo, M. Eyes hint at hidden mental-health conditions. *Eyes hint at hidden mental-health*

1164   *conditions* https://www.nature.com/articles/d41586-019-01114-9 (2019).

1165   78. Tahsili-Fahadan, P. & Geocadin, R. G. Heart–Brain Axis. *Circulation Research* **120**, 559–

1166   572 (2017).

1167   79. Leng, F. & Edison, P. Neuroinflammation and microglial activation in Alzheimer disease:

1168   where do we go from here? *Nat Rev Neurol* **17**, 157–172 (2021).

1169   80. Murphy, C. E., Walker, A. K. & Weickert, C. S. Neuroinflammation in schizophrenia: the

1170   role of nuclear factor kappa B. *Transl Psychiatry* **11**, 1–13 (2021).

1171   81. Miller, A. H. & Raison, C. L. The role of inflammation in depression: from evolutionary

1172   imperative to modern treatment target. *Nat Rev Immunol* **16**, 22–34 (2016).

1173   82. Tan, A. H., Lim, S. Y. & Lang, A. E. The microbiome–gut–brain axis in Parkinson disease

1174   — from basic research to the clinic. *Nat Rev Neurol* **18**, 476–495 (2022).

1175   83. Morais, L. H., Schreiber, H. L. & Mazmanian, S. K. The gut microbiota–brain axis in

1176   behaviour and brain disorders. *Nat Rev Microbiol* **19**, 241–255 (2021).

51

1177 84. Tost, H., Champagne, F. A. & Meyer-Lindenberg, A. Environmental influence in the brain,

1178   human welfare and mental health. *Nat Neurosci* **18**, 1421–1431 (2015).

1179 85. UKBB, U. Ambitious project announced to create the world's largest longitudinal imaging

1180   dataset. https://www.ukbiobank.ac.uk/learn-more-about-uk-biobank/news/ambitious-

1181   project-announced-to-create-the-world-s-largest-longitudinal-imaging-dataset.

1182 86. Wang, R., Chaudhari, P. & Davatzikos, C. Embracing the disharmony in medical imaging:

1183   A Simple and effective framework for domain adaptation. *Med Image Anal* **76**, 102309

1184   (2022).

1185 87. Varol, E., Sotiras, A. & Davatzikos, C. HYDRA: Revealing heterogeneity of imaging and

1186   genetic patterns through a multiple max-margin discriminative analysis framework.

1187   *NeuroImage* **145**, 346–364 (2017).

1188 88. Tustison, N. J. *et al.* N4ITK: improved N3 bias correction. *IEEE Trans. Med. Imaging* **29**,

1189   1310–1320 (2010).

1190 89. Doshi, J. *et al.* MUSE: MUlti-atlas region Segmentation utilizing Ensembles of registration

1191   algorithms and parameters, and locally optimal atlas selection. *Neuroimage* **127**, 186–195

1192   (2016).

1193 90. Manichaikul, A. *et al.* Robust relationship inference in genome-wide association studies.

1194   *Bioinformatics* **26**, 2867–2873 (2010).

1195 91. Price, A. L., Zaitlen, N. A., Reich, D. & Patterson, N. New approaches to population

1196   stratification in genome-wide association studies. *Nat Rev Genet* **11**, 459–463 (2010).

1197 92. Abraham, G., Qiu, Y. & Inouye, M. FlashPCA2: principal component analysis of Biobank-

1198   scale genotype datasets. *Bioinformatics* **33**, 2776–2778 (2017).

1199   93. Purcell, S. *et al.* PLINK: A Tool Set for Whole-Genome Association and Population-Based

1200   Linkage Analyses. *Am J Hum Genet* **81**, 559–575 (2007).

1201   94. Watanabe, K., Taskesen, E., van Bochoven, A. & Posthuma, D. Functional mapping and

1202   annotation of genetic associations with FUMA. *Nat Commun* **8**, 1826 (2017).

1203   95. The GTEx Consortium. The Genotype-Tissue Expression (GTEx) project. *Nat Genet* **45**,

1204   580–585 (2013).

1205   96. Bulik-Sullivan, B. *et al.* An atlas of genetic correlations across human diseases and traits.

1206   *Nat Genet* **47**, 1236–1241 (2015).

1207   97. Bowden, J. *et al.* A framework for the investigation of pleiotropy in two-sample summary

1208   data Mendelian randomization. *Stat Med* **36**, 1783–1802 (2017).

1209   98. Bowden, J., Davey Smith, G. & Burgess, S. Mendelian randomization with invalid

1210   instruments: effect estimation and bias detection through Egger regression. *Int J Epidemiol*

1211   **44**, 512–525 (2015).

1212   99. Ge, T., Chen, C.-Y., Ni, Y., Feng, Y.-C. A. & Smoller, J. W. Polygenic prediction via

1213   Bayesian regression and continuous shrinkage priors. *Nat Commun* **10**, 1776 (2019).

1214   100. Wen, J. *et al.* Convolutional neural networks for classification of Alzheimer's disease:

1215   Overview and reproducible evaluation. *Medical Image Analysis* **63**, 101694 (2020).

1216   101. Nadeau, C. & Bengio, Y. Inference for the Generalization Error. *Machine Learning* **52**,

1217   239–281 (2003).

1218   102. Wen, J. MEDICINE: AI-derived GWAS summary statistics sharing portal. (2025)

1219   doi:https://doi.org/10.7303/syn64923248.

1220   103. Wen, J. MLNI (Version 0.1.4) [Computer software]. (2025)

1221   doi:https://github.com/anbai106/mlni.

53

1222   104. Yang, Z. Surreal-GAN (Version 0.1.1) [Computer Software]. (2025)

1223   doi:https://github.com/zhijian-yang/SurrealGAN.

1224